POLITECNICO
MILANO 1863

SCUOLA DI INGEGNERIA INDUSTRIALE
E DELL'INFORMAZIONE

Strain Engineering in WSe_2 monolayer for Single Photon Emission

Tesi di Laurea Magistrale in
Materials Engineering and Naontechnologies -
Ingegneria dei Materiali e Nanotecnologie

Author: **Thomas Fantin**

Student ID: 252223
Advisor: Prof. Carlo Spartaco Casari
Co-advisors: Pablo Hernandez Lopez and Dr. Sebastian Heeg
Academic Year: 2024-25

Abstract

Single–photon sources are a key component for the development of quantum photonic technologies. Among the different solid–state platforms, strained monolayers of transition metal dichalcogenides, and in particular WSe_2, have emerged as promising candidates due to their strong excitonic response and compatibility with planar device architectures. This work investigates strain–induced hybridization between dark excitons and interband defect–related states as the potential key mechanism behind single-photon emission in WSe_2. Within this framework, strain engineering is explored as a route to activate and control localized quantum emitters.

Localized strain is introduced via contaminant–induced nanobubbles formed in WSe_2/MoS_2 stacks. Multilayer MoS_2 substrates are employed to quench photoluminescence in unstrained regions of WSe_2 through type-II band alignment. A systematic fabrication protocol is developed, involving mechanical exfoliation of WSe_2 monolayers onto PDMS, transfer onto multilayer MoS_2 substrates, and subsequent annealing to promote nanobubble formation and localized strain. A central result of this work is the experimental observation that the average strain induced within WSe_2 nanobubbles depends on the thickness of the MoS_2 substrate. This dependence is attributed to changes in the adhesion forces between the WSe_2 monolayer and the substrate as the number of MoS_2 layers increases, which in turn modify the bubble shape and lead to variations in the induced strain. In addition, a bubble patterning approach based on laser writing of the underlying PDMS is explored, where localized heating above a threshold in laser frequency and power triggers deterministic bubble nucleation.

The strain distribution within nanobubbles is characterized beyond the diffraction limit using tip–enhanced photoluminescence, enabling nanoscale correlation between local strain and optical response. Cryogenic confocal photoluminescence measurements are performed to investigate the conditions required for the onset of single–photon emission.

The experimental observations are discussed in the context of the proposed strain–driven hybridization mechanism. Finally, perspectives toward deterministic strain engineering and scalable integration of WSe_2–based single–photon emitters in photonic devices are outlined.

Keywords: Single-photon emitters, WSe_2 monolayers, Substrate adhesion, Nanobubble patterning, Tip-enhanced spectroscopy, Strain-driven hybridization.

Abstract in lingua italiana

Le sorgenti a singolo fotone rappresentano un elemento fondamentale per lo sviluppo delle tecnologie fotoniche quantistiche. Tra le diverse piattaforme allo stato solido, i monostrati sottoposti a strain di dicalcogenuri dei metalli di transizione, e in particolare il WSe_2, sono emersi come candidati promettenti grazie alla loro forte risposta eccitonica e alla compatibilità con architetture di dispositivi planari. In questo lavoro, l'emissione a singolo fotone in monostrati di WSe_2 viene studiata ipotizzando che essa abbia origine da un'ibridazione indotta dallo strain tra eccitoni scuri e stati localizzati associati a difetti. In tale contesto, l'ingegneria dello strain viene esplorata come strategia per attivare e controllare emettitori quantistici localizzati.

Lo strain localizzato viene introdotto tramite nanobolle indotte da contaminanti, formate in eterostrutture WSe_2/MoS_2. Substrati di MoS_2 multistrato vengono utilizzati per sopprimere la fotoluminescenza nelle regioni non deformate del WSe_2 attraverso un allineamento di banda di tipo II. Viene sviluppato un protocollo di fabbricazione sistematico che comprende l'esfoliazione meccanica di monostrati di WSe_2 su PDMS, il trasferimento su substrati di MoS_2 multistrato e una successiva fase di annealing per favorire la formazione delle nanobolle e dello strain localizzato. Un risultato centrale di questo lavoro è l'osservazione sperimentale che lo strain medio indotto all'interno delle nanobolle di WSe_2 dipende dallo spessore del substrato di MoS_2. Tale dipendenza è attribuita a variazioni delle forze di adesione tra il monostrato di WSe_2 e il substrato all'aumentare del numero di strati di MoS_2, che modificano la forma delle bolle e determinano differenti livelli di strain indotto. Inoltre, viene esplorato un approccio di patterning delle bolle basato sulla scrittura laser del PDMS sottostante, in cui un riscaldamento localizzato al di sopra di una soglia di frequenza e potenza del laser innesca la nucleazione deterministica delle bolle.

La distribuzione di strain all'interno delle nanobolle viene caratterizzata oltre il limite di diffrazione mediante fotoluminescenza potenziata da punta, consentendo una correlazione su scala nanometrica tra strain locale e risposta ottica. Misure di fotoluminescenza a temperature criogeniche vengono infine eseguite per indagare le condizioni necessarie all'insorgenza dell'emissione a singolo fotone.

I risultati sperimentali vengono discussi alla luce del meccanismo di ibridazione indotto dallo strain proposto. In conclusione, vengono delineate le prospettive per un'ingegneria dello strain deterministica e per l'integrazione scalabile di emettitori a singolo fotone basati su WSe_2 in dispositivi fotonici.

Parole chiave: Emettitori a singolo fotone, Monolayer di WSe_2, Adesione al substrato, Patterning di nanobolle, Spettroscopia tip–enhanced, Ibridazione indotta da deformazione.

Contents

Introduction

The development of scalable quantum technologies represents one of the most ambitious scientific and engineering challenges of the twenty-first century. Among the fundamental building blocks required for quantum communication, quantum computing, and quantum cryptography, single-photon sources play a central role for what concerns qbit transport at long distances. The ability to generate on-demand, indistinguishable single photons with high purity and efficiency is essential for the implementation of secure quantum key distribution protocols, linear optical quantum computing schemes, and integrated photonic quantum circuits [48, 49].

Single-photon emitters include solid-state systems, like quantum dots, Nitrogen-vacancies in diamond and 2D materials [53], atomic and molecular emitters, and probabilistic nonlinear-optical sources [17].
Within this landscape, 2D materials, like hBN, GaSe or transition metal dichalcogenides (WSe_2, MoS_2, WS_2 and $MoSe_2$), provide the implementation of single–photon emitters in planar devices [44]. In particular, transition metal dichalcogenides (TMD) monolayers have attracted significant interest due to their exceptional optical properties related to strong excitonic effects [56]. WSe_2 is preferred over TMDs because it provides the most reproducible and controllable single-photon emission, with spectrally clean lines and strong compatibility with strain engineering and van der Waals heterostructures [44, 45, 53].

When thinned down to the monolayer limit, TMDs undergo a transition from an indirect to a direct bandgap semiconductor, resulting in strong photoluminescence dominated by tightly bound excitonic complexes [56]. The reduced dielectric screening and quantum confinement in two dimensions lead to large exciton binding energies, making TMDs highly sensitive to external perturbations such as strain, temperature, and dielectric environment [2, 23, 53, 56].

As anticipated earlier, a remarkable phenomenon observed in WSe_2 monolayers is the emergence of narrow and intense emission lines at cryogenic temperatures, exhibiting photon antibunching and therefore single-photon emission (SPE) [53]. Despite extensive experimental and theoretical investigations, the exact origin of single-photon emission in

WSe_2 monolayers remains an open question.
These single–photon emitters are typically localized at nanoscale regions where the electronic structure is modified by local perturbations [14]. Among the various strategies explored to induce and control such localized emission, strain engineering has emerged as a particularly powerful and versatile approach.

Mechanical strain modifies the lattice constant and orbital overlap in WSe_2, leading to bandgap renormalization and the formation of local potential minima [20]. In the presence of nonuniform strain distributions, excitons are funneled toward regions of maximum tensile strain, where they can become spatially confined [27]. In this context, strain-induced hybridization between dark exciton states and defect-related electronic states has been proposed as a possible microscopic mechanism enabling efficient radiative recombination from otherwise optically forbidden transitions [23, 31].

Different methods have been developed to introduce local strain in a controlled manner, including nanopillar substrates and contaminant-induced nanobubbles [41, 46]. In particular, nanobubbles formed between a WSe_2 monolayer and an underlying substrate generate strong and highly localized strain fields, producing confinement potentials capable of activating SPE. This approach offers a relatively simple fabrication route, and also the possibility to tune the strain induced in the single nanobubble by changing the substarte, as it will be showed in Chapter 3. More specifically, within this work, strain engineering in WSe_2 monolayers stacked on multilayer MoS_2 substrates with contaminant nanobubbles at their interface is investigated as a platform for single-photon emission. The multilayer MoS_2 plays a dual role: it induces photoluminescence quenching in unstrained regions via type-II band alignment, thereby enhancing the contrast of strained sites [45], and it enables tuning of the adhesion and strain magnitude by varying its thickness.

The main objective of this thesis is to explore the correlation between local strain, induced by nanobubbles, and the occurrence of single-photon emission in WSe_2 monolayers. In particular, the hypothesis that SPE originates from enhanced emission of light due to strain-driven hybridization between dark excitons and defect-related states is examined. To this end, photoluminescence spectroscopy at room and cryogenic temperatures is combined with atomic force microscopy and tip-enhanced photoluminescence mapping, allowing nanoscale investigation of the strain distribution beyond the diffraction limit.
By systematically analyzing the optical response of nanobubbles formed on substrates with different MoS_2 thicknesses, this work aims to identify the strain range associated with the activation of SPE and to evaluate the possibility of deterministic strain control through substrate engineering.
Furthermore, in this work, a PDMS-based nanobubble patterning approach is investi-

gated, in which laser writing is used to locally modify the PDMS substrate and deterministically define the nucleation sites of strain-inducing bubbles. This strategy represents a promising route toward the realization of scalable arrays of single-photon emitters with controlled positioning and improved uniformity.

1 | Two dimensional materials and their optical properties

Single-photon emission is a physical phenomenon of significant interest, as single-photon sources can be integrated into photonic circuits for quantum computing and quantum information applications. Among the material platforms capable of exhibiting this behavior, atomically thin transition metal dichalcogenides (TMDs), in particular WSe_2 monolayers, are found.

This chapter introduces the atomic and electronic structure of TMDs, both in bulk and monolayer form, and discusses their response to external parameters such as temperature and strain. It then focuses on the phenomenon of single-photon emission and on the hypotheses proposed to explain its origin in WSe_2 monolayers. This framework provides the theory necessary to interpret the experimental results presented in Chapters 3 and 4.

1.1. Monolayer Transition Metal Dichalcogenides (TMDs)

This section introduces the theoretical background of the band structure of TMDs, with particular emphasis on their monolayer form. Understanding their electronic structure is essential to interpret their optical properties, including photoluminescence emission and Raman scattering. The fundamental principles of these far-field, confocal techniques are presented in the second part of the section.

1.1.1. TMDs: 2D Semiconductors

Transition metal dichalcogenides (TMDs) are layered materials with chemical formula AB_2, where A is a transition metal, typically Mo or W, and B is a chalcogen element such as S, Se or Te [56]. A TMD monolayer consists of three atomic planes arranged in an B–A–B configuration, with the transition-metal atoms occupying the central plane and the chalcogen atoms located in two planes above and below, as displayed in Figure 1.1-a [56]. Within each layer, atoms are bound by strong covalent interactions, while adjacent layers

are held together by weak van der Waals forces. This anisotropic bonding allows mechanical exfoliation, a technique in which thin flakes up to the monolayer limit are peeled from a bulk layered crystal using adhesive tape [40]. Such technique allows the isolation of TMD monolayers through a simple and cheap process [8], and it was used to produce the samples involved in this work, as discussed in Section 2.1.1.
Many commonly studied semiconducting TMDs, such as MoS_2, WS_2, $MoSe_2$ and WSe_2, crystallize predominantly in the 2H phase, which exhibits hexagonal symmetry (Fig. 1.1-a), thus also their Brillouin zone is hexagonal [57], having high symmetry points Γ, K, K', M and Q, represented in Figure-1.1-b.

When approaching the monolayer limit in TMDs, a transition of the band gap from indirect to direct occurs (Fig. 1.1-c,d), leading to enhanced absorption and emission of light in TMD monolayers [34]. In bulk crystals, TMDs are indirect semiconductors, where the relevant band extrema involve states near the Γ point at the center of the hexagonal Brillouin zone (Fig. 1.1-c). These states, unlike those at the K points located at the zone corners, are strongly affected by interlayer hybridization. As a result, the electronic transitions associated with Γ are highly sensitive to the number of layers and differ fundamentally between bulk and monolayer samples, where interlayer coupling is absent. In contrast, the transitions at the K valleys involve orbitals localized within the inner atomic plane and remain nearly unchanged with thickness [6].

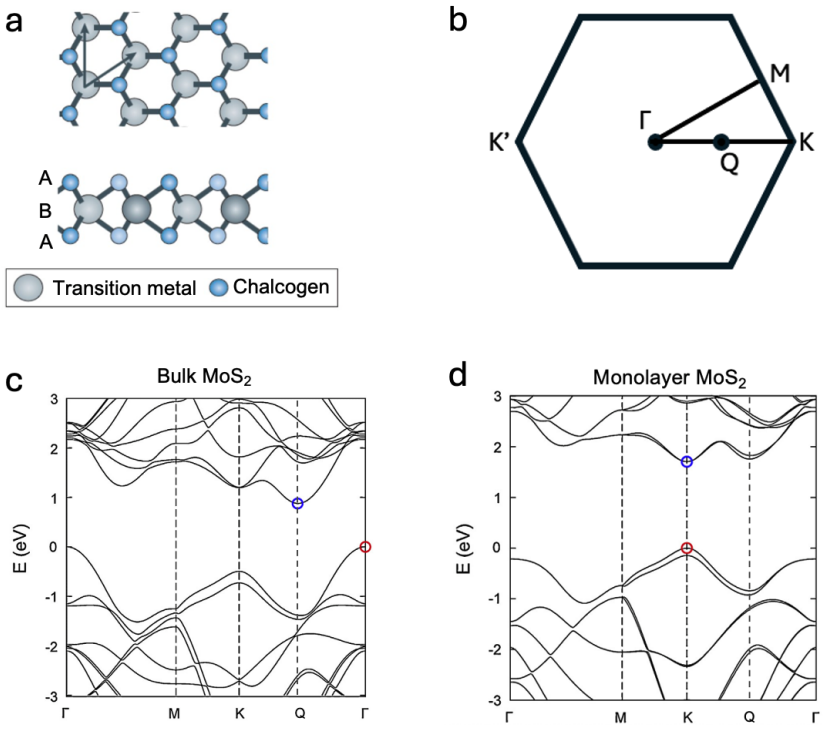

Figure 1.1: **TMDs crystalline and band structures.** (a) Configuration of transition metal and chalcogen atoms within a single layer of a generic TMD. The monolayer has hexagonal translational symmetry. Adapted from [37]. (b) Hexagonal Brillouin zone of a TMD. High symmetry points, namely K,K',Γ,M and Q, are reported. Bulk (c) and monolayer (d) band structures of a TMD, namely molybdenum disulfide. It is shown how the bandgap is direct for monolayer MoS_2, unlike bulk MoS_2. Taken from [59].

When TMDs are irradiated with photons having energy larger than the bandgap, photoexcited electrons and holes bind through Coulomb attraction to form excitons, quasiparticles that dominate the optical response of TMDs. A neutral exciton consists of one electron and one hole, while in the presence of excess carriers an exciton can bind an additional charge to form a trion, either negative or positive one depending on the doping (Fig. 1.2-a). The energy that is required to separate the constituent carriers is called the binding energy, E_B, while the energy difference of exciton and trion is called the trion dissociation energy, E_{diss} (Fig. 1.2-b). Owing to the reduced dielectric screening and two–dimensional confinement, these excitonic complexes have very strong binding energy, of few hundreds of meV, and therefore govern optical properties in TMDs [60].

In addition, defects in TMDs, such as vacancies or impurities, can introduce electronic states within the band gap, often referred to as intragap or defect–related states, represented in Figure 1.2-b. These localized levels act as trapping centers for charge carriers,

giving rise to additional optical transitions at energies below the exciton resonance [58].

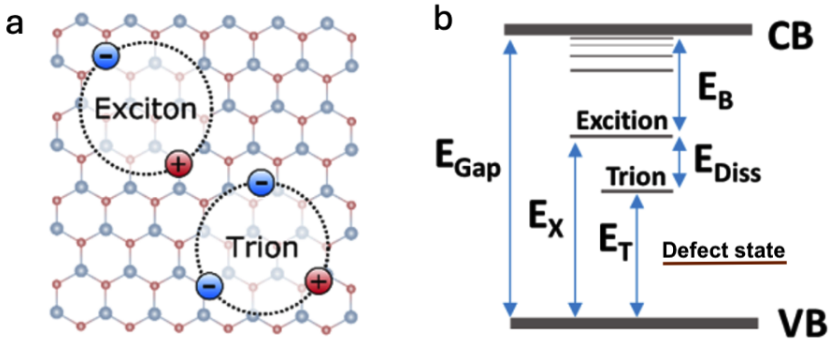

Figure 1.2: **Interband energy levels in TMDs.** (a) Schematic representation of a neutral exciton and a trion within an hexagonal lattice. The neutral exciton is a quasi-particle obtained by the Coulomb interaction between a hole and an electron, while a trion involves three particles. (b) Display of energy position of excitons and defect related states inside the bandgap. Adapted from [32].

Another characteristic physical property of TMDs is the spin splitting of electronic bands at the band edges. The crystal symmetry, combined with the strong spin–orbit interaction originating from the heavy transition–metal atoms, lifts the spin degeneracy of both conduction and valence bands around the K valleys and introduces the valley degree of freedom (Fig. 1.3-a), allowing optical transitions only between valleys with the same spin orientation, as displayed in Figure 1.3-b [56].
As a consequence of this selection rule, dark bands, and so dark excitons, are found in the electronic structure of TMDs monolayers (Fig. 1.3-b). A dark exciton is an excitonic state that cannot recombine radiatively under direct optical excitation because the transition is forbidden by spin selection rules and/or by momentum conservation. Such states can still be populated through scattering processes [56].

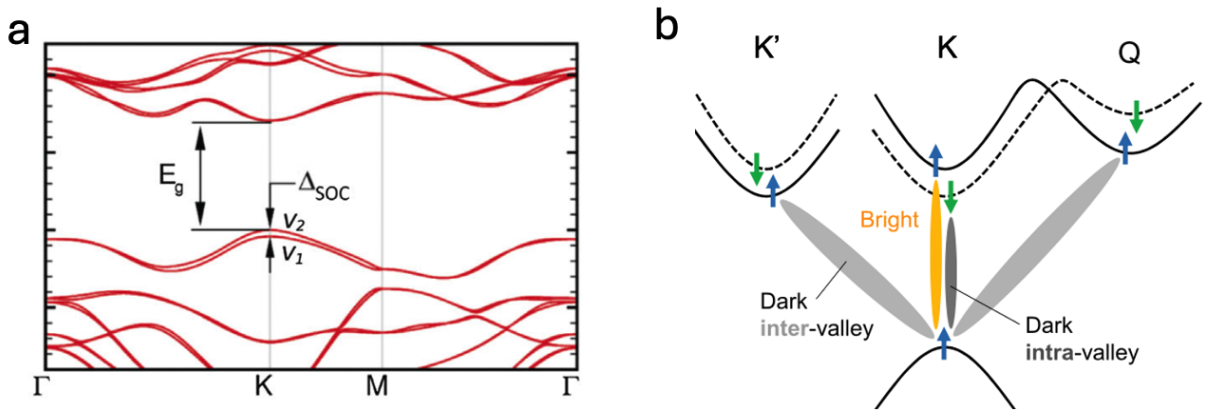

Figure 1.3: **Spin–orbit coupling optical selection rule in TMDs.** (a) Typical band structure for TMD monolayers calculated using density functional theory: valley splitting (v_1, v_2) related to spin–orbit coupling can be visualized at the top of the valence band. (b) Allowed recombination mechanism: even though the dark intra–valley transition is the one requiring least energy, it is not allowed due to spin–orbit coupling. Taken from [56].

1.1.2. TMDs heterobilayers

A TMD heterobilayer is created by stacking two TMD crystals so that they interact through van der Waals coupling. The two materials align their band edges and work functions such that electrons and holes occupy their lowest–energy states in different layers. This band arrangement effectively forms an atomically thin pn junction, in which optically generated carriers undergo ultrafast interlayer charge transfer and become spatially separated. Such band configuration is called Type II band alignment [45]. Since the charges involved in recombination are spatially separated, radiative recombination is inhibited. Thus, in the areas in which two different TMDs are in contact, photoluminescence is quenched.

1.1.3. Optical fingerprint of TMDs

Photoluminescence (PL) and Raman spectroscopy were employed as the main optical characterization techniques in this work, as they provide access to the electronic and vibrational properties of TMD semiconductors. Photoluminescence probes radiative electronic transitions and allows the identification of electronic energy levels in the crystal, while Raman spectroscopy is sensitive to lattice vibrational modes.
As shown in Figure 1.4–a, both Raman and photoluminescence signals are obtained by illuminating the sample with an excitation laser and by collecting the light emitted or scattered by the sample. For this reason, both techniques were implemented using the

same experimental setups, described in Section 2.3.

More specifically, In PL spectroscopy, photons from the excitation beam are absorbed by the sample and promote electrons to higher-energy electronic states. After this, radiative recombination occurs, leading to the emission of photons at lower energy than the excitation light. The emitted spectrum therefore reflects the electronic structure of the material within the irradiated area (Fig. 1.4-a).
In TMDs, where optical properties are dominated by excitonic effects, PL measurements directly probe the energy of these bound states within the bandgap. As WSe_2 is the TMD mainly involved in this work, the PL spectrum of an unstrained WSe_2 monolayer is shown in Figure 1.4–b, where the emission results from the combination of two excitonic contributions: the neutral exciton (X_0) and the trion (X_T) [52].

Raman spectroscopy is instead based on the inelastic scattering of photons by lattice vibrations. When the excitation beam interacts with a material, electrons are excited to a virtual energy state. While most photons are elastically scattered (Rayleigh scattering), a small fraction undergoes inelastic scattering, exchanging energy with vibrational modes of the lattice. In the Stokes process, the scattered photon loses energy by creating a phonon, whereas in the Anti-Stokes process the photon gains energy by annihilating a phonon already present in the lattice, as showed in Figure 1.4–a. In TMDs, the main vibrational modes whose signal can be detected by Raman spectroscopy are the A_{1g} mode, associated with the out–of–plane vibrations of chalcogen atoms, and the E_{2g} mode originated from in–plane vibrations within a single layer, represented in Figure 1.4-c [29].

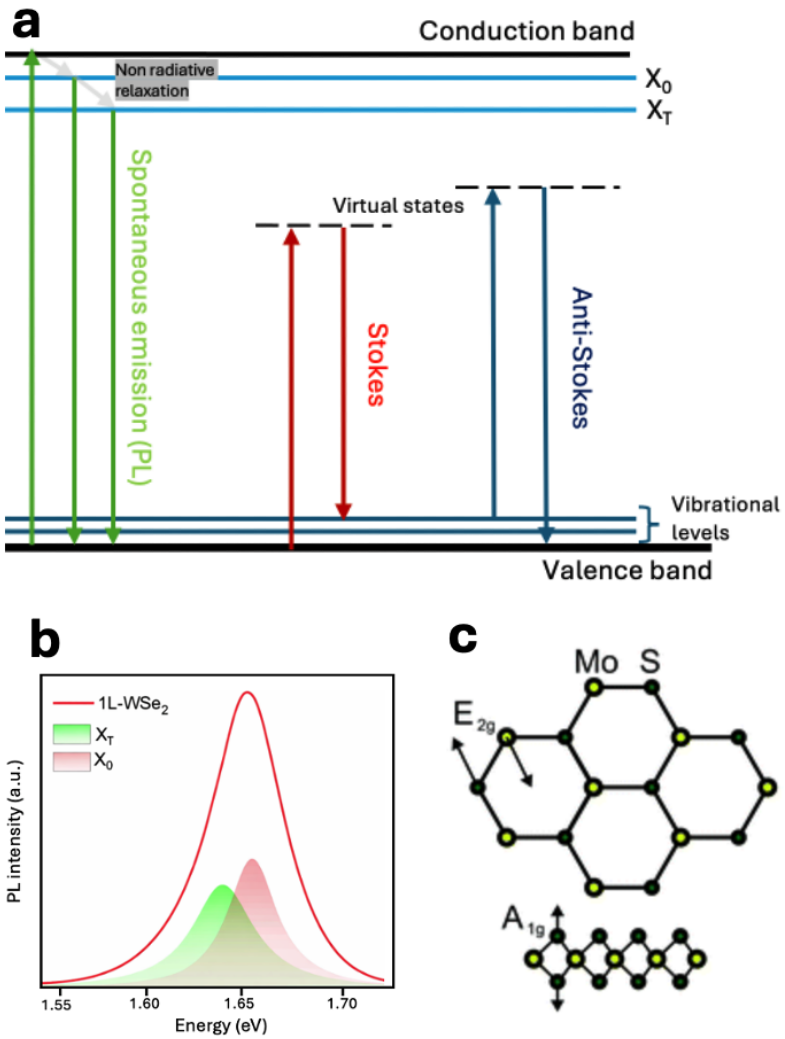

Figure 1.4: **Photoluminescence and Raman spectroscopy in TMDs.** (a) Schematic representation of radiative recombinations giving photoluminescence, and inelastic scattering processes (Stokes and anti-Stokes), responsible of Raman spectroscopy. (b) PL emission spectrum of an unstrained WSe_2 monolayer, the total distribution is the sum of emission related to the neutral exciton (X_0) and the trion (X_T). Adapted from [10]. (c) Schematic representation of E_{2g} and A_{1g} vibrational modes in a monolayer of MoS_2. Taken from [36].

1.2. Strain and temperature dependence of the optical properties in WSe_2 monolayers

This section discusses the influence of external parameters, such as temperature and strain, on the optical emission properties of WSe_2 monolayers, the TMD primarily investigated in this work. This is done as Single–photon emission in WSe_2 monolayers is reported to

occur under tensile strain conditions and at cryogenic temperatures [53].

First, the effect of temperature on photoluminescence is examined, with particular emphasis on thermally induced redshift and peak broadening. Subsequently, the impact of strain is addressed, as it leads to a reduction of the optical bandgap and may induce hybridization processes between interband electronic states.

1.2.1. Change in optical properties in WSe_2 monolayers with temperature

With decreasing temperature, the band gap of TMDs generally increases. This behavior is mainly due to lattice thermal expansion and electron–phonon interactions, which reduce the band gap at elevated temperatures. Upon cooling, the suppression of these effects leads to a widening of the band gap and a consequent blueshift of the excitonic transitions, as shown in Figure 1.5 [2].

At the same time, reduced phonon scattering at low temperatures leads to significant linewidth narrowing. In WSe_2 monolayers, as the temperature is reduced, not only the neutral exciton and trion peaks, marked respectively as 1 and 2 in Figure 1.5, become clearly distinguishable, but additional emission features also emerge at energies lower than the main excitonic transitions (3,4). Although their microscopic origin is still under debate, such energy levels are commonly attributed to defect-related or localized states discussed in Section 1.1.1 [24]. These states are thermally quenched at high temperatures, as the thermal energy exceeds the binding energy of such states, enabling exciton delocalization and activation of non-radiative recombination channels [24].

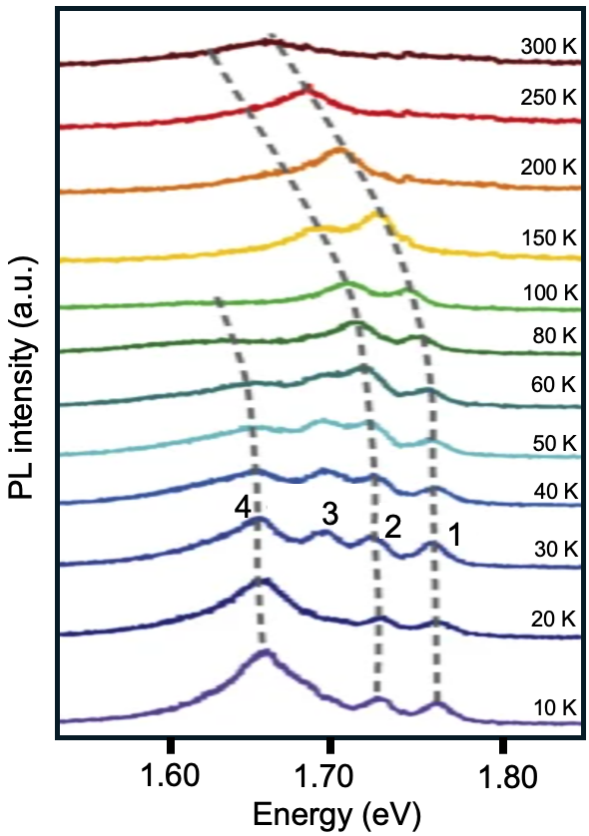

Figure 1.5: **PL spectra of unstrained WSe_2 at low temperatures.** While at room temperature (300 K), the spectrum is the sum of trion and neutral exciton peaks, going at lower temperatures (80K or less) new peaks can be identified. At T=50 K, neutral exciton and trion peaks are marked as 1 and 2 respectively, while the peaks related to localized states are marked as 3 and 4. Dashed lines trace the thermally induced redshift of exciton peaks. Adapted from [24].

1.2.2. Strain-related effects on electronic properties

In monolayer WSe_2, applied strain, namely the mechanical deformation that stretches or compresses a material, modifies the lattice constant and orbital overlap, which alters the electronic band structure. Tensile strain typically lowers the conduction-band minimum and raises the valence-band maximum, reducing the band gap. This results in a redshift of the excitonic optical transitions observed in photoluminescence [20, 23]. The WSe_2 PL dependency on strain is being reported in Figure 1.8-a.

In the presence of nonuniform strain in a WSe_2 monolayer, spatial minima in the conduction band and maxima in the valence band are formed. This creates an effective energy landscape that drives excitons toward regions of highest strain, where the band gap is smaller. As a result, excitons funnel into these low-energy areas, as schematically illus-

trated in Figure 1.8-b. Exciton funneling is limited by the finite exciton diffusion length, which is determined by the exciton lifetime and mobility and is reduced by exciton–phonon scattering and disorder [27].

As displayed in Figure 1.6-c, as strain is increased in WSe_2 monolayers, the dark–exciton level (X_d^0) is brought into resonance with the defect–related states, leading to hybridization in between those states, and thus to avoided crossings in energy. The hybrid states overcome the spin–orbit coupling selection rule described in Section 1.1.1, enhancing radiative recombination [23, 31].
This resonant mixing occurs for approximately 1% tensile strain and then again at 2.5%, as hybridization can occur with two different interband defect-related energy levels, namely D1 and D2.
As reported in Figure 1.6-a, for 1% strain the PL spectrum splits in two peaks, due to avoided crossing of the states. As the strain is increased furthermore, an intensification of PL occurs, related to the SOC optical selection rule relaxation.

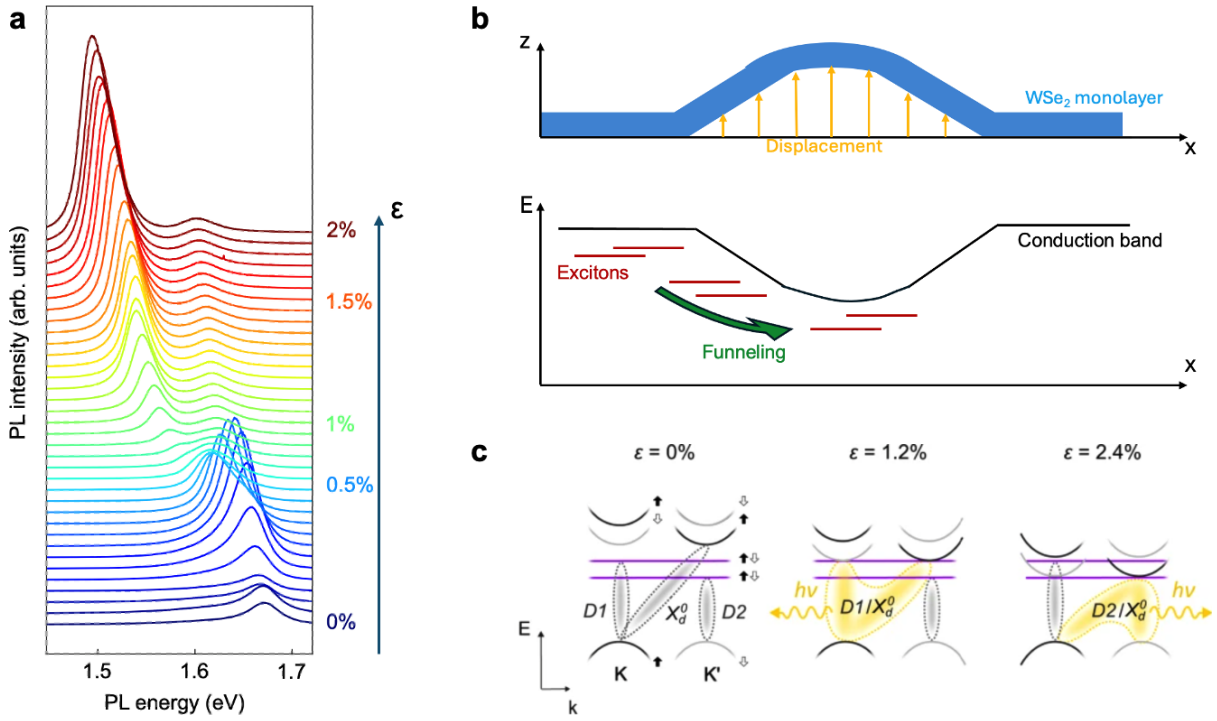

Figure 1.6: **Strain effect on WSe_2 monolayers.** (a) PL spectrum dependence on strain at room temperature: the intensity maxima redshifts with tensile strain. Provided by Pablo Hernandez Lopez and Sebastian Heeg. (b) Exciton funneling due to strain gradient. (c) Schematic representation of strain-driven hybridization occurring at two strain levels. Efficient radiative recombination is allowed as such hybridization overcomes spin–orbit couplung selection rule. Taken from [23].

1.3. Single Photon Emission in strained WSe_2 monolayers

In this section a physical description of single-photon emission is first introduced, together with the key performance metrics that define a high-quality single-photon source, namely brightness, photon indistinguishability, and single-photon purity.
An overview of the current state of the art in solid-state single-photon sources is then presented, including strained WSe_2 monolayers among the relevant material platforms.
Finally, the hypothesis proposed to explain single-photon emission in strained WSe_2 monolayers is discussed, along with the main strategies used to induce strain in atomically thin WSe_2.

1.3.1. Single–photon emission: definition, characterization and performance criteria

Single-photon emission (SPE) is a natural quantum process in which a single quantum system emits one and only one photon at a time during an energy transition. After emission, the system must be re-excited before another photon can be produced.
A single–photon source can be implemented in quantum communications if it can generate pulses of single photons on demand, one-by-one, and such that all emitted photons are identical in all relevant degrees of freedom, namely polarization, spectral shape, temporal mode shape, spatial mode shape [18].
As a result, the PL spectrum of a single-photon emitter exhibits few µeV narrow and intense emission lines at well-defined wavelengths, corresponding to the discrete energy levels responsible for such radiative transitions [53].

The performance metrics commonly used to characterize a single-photon source are the following [48].

- Single–photon purity: it measures how often the source emits only one photon, without multi-photon contributions. Single–photon purity is established measuring the second order intensity correlation function $g^{(2)}(\tau)$, defined as the probability to detect two photons coming from the same source within a time interval τ.
  An ideal single–photon source should have $g^{(2)}(0) = 0$, however a device is considered to be a single–photon emitter for $g^{(2)}(0) < 0.5$ [30].
- Photon indistinguishability: it quantifies how identical two single-photon quantum states are. It is defined as the wavepacket overlap in between the two photons:

$M = |\langle\psi_1|\psi_2\rangle|^2$. Perfect indistinguishability ($M = 1$) occurs when the two photons are in the same pure quantum state. Photon indistinguishability is measured using Hong–Ou–Mandel (HOM) interference. Two photons are injected into the two input ports of a 50:50 beam splitter. The coincidence rate between the two output detectors is measured as a function of time delay. Indistinguishable photons interfere and exit together, suppressing coincidences causing the detection of an "HOM dip". The HOM visibility extracted from second-order correlations gives the indistinguishability M. [48].

- Brightness: it measures the probability of obtaining a single photon per impulse. It is defined as the single photon detection rate over the laser repetition rate, i.e. the frequency at which a pulsed laser emits successive optical pulses. [48].

In addition to this, to be implemented in quantum circuits, a single-photon emitter must be compatible with scalable device architectures and with cost-effective fabrication [49].

1.3.2. Comparison of devices hosting Single Photon Emission

The development of efficient and scalable single-photon emitters (SPEs) has become a central objective in quantum photonic technologies. To date, several solid state platforms have emerged as leading candidates, spanning different dimensionalities: zero-dimensional semiconductor quantum dots, bulk defects in wide-bandgap crystals, and atomically thin two-dimensional materials. Each of these systems offers distinct advantages and limitations, reported in Table 1.1, which define the current landscape of solid-state single-photon sources [53].

A quantum dot is a nanoscale semiconductor structure that confines charge carriers in all three spatial dimensions, leading to discrete, atom-like energy levels. As a single-photon emitter, a quantum dot works by optical or electrical excitation followed by radiative recombination of an electron–hole pair, emitting one photon per excitation cycle. Quantum dots currently provide the highest performance in terms of photon indistinguishability and brightness when integrated into photonic cavities, although they typically require cryogenic operation [47].
Another well established single–photon source are nitrogen-vacancy (NV) centers, namely point defects in diamond consisting of a substitutional nitrogen atom adjacent to a lattice vacancy, forming a localized quantum system. As single-photon emitters, NV centers emit photons through optical excitation of electronic states followed by radiative decay, with the emitted photons properties linked to orbital structure of the defects. NV centers in diamond stand out for their robustness and room-temperature operation, but suffer from

limited photon indistinguishability without additional cavity engineering [15].
Single-photon emitters based on WSe_2 monolayers stand out among 2D single–photon sources for their excellent single-photon purity at low temperature and unique advantages in site control and integration with planar nanophotonic platforms. However, their performance is still limited by fluctuations of the local electrostatic environment, which cause spectral diffusion of the emission line, as well as by exciton–phonon interactions that induce dephasing and broaden the optical transition. This currently constrains photon indistinguishability and high-temperature operation [53].

Table 1.1: Comparison of solid-state single-photon emitter platforms.

	Quantum Dots	**NV (Diamond)**	**WSe_2 (2D)**
Single-photon purity	Very high ($g^{(2)}(0) \ll 0.5$)	High	Very high
Indistinguishability	Near-unity	Limited	Limited
Brightness	Very high	Moderate–high	Moderate
Implementability	Mature photonic integration	Robust, spin-addressable	Excellent planar integration
Operating temperature	Cryogenic (few K)	Up to room T	< 10 K

1.3.3. Strained WSe_2 monolayer-based devices

Strain engineering in monolayer WSe_2 has emerged as a powerful strategy to realize SPEs. Local strain modifies the band structure by reducing the bandgap in confined regions, thereby creating low-energy potential pockets. Excitons generated in the surrounding area can drift toward these minima through exciton funneling, where they accumulate and recombine radiatively (Fig. 1.7-a). As a consequence, the photoluminescence spectrum exhibits sharp and intense emission lines at well-defined energies (Fig. 1.7-b), typically observed at cryogenic temperatures ($T < 10$ K) [1], where thermal-induced broadening is suppressed.

A widely discussed hypothesis attributes SPE in strained WSe_2 to strain-induced hybridization between dark excitonic states and defect-related electronic states, discussed in Section 1.2.2. In pristine monolayers, strong spin–orbit coupling renders the lowest-energy exciton optically dark. However, strain–driven reduction of the bandgap can mix dark excitons with defect states, partially relaxing optical selection rules and enabling efficient, spatially confined radiative recombination. This hybridization is believed to be responsible for antibunched emission [31].
An alternative interpretation attributes single-photon emission in monolayer WSe_2 primarily to defect-bound excitons. In this picture, intrinsic or extrinsic lattice defects introduce localized electronic states within the bandgap, which act as trapping centers for excitons. The strong spatial confinement provided by these defect states gives rise

to discrete, atom-like optical transitions, resulting in spectrally sharp emission lines and photon antibunching [13].

This work seeks to shed light on the mechanism responsible for single-photon emission, exploring the possibility that it arises from strain-induced hybridization between dark excitons and defect-related states.

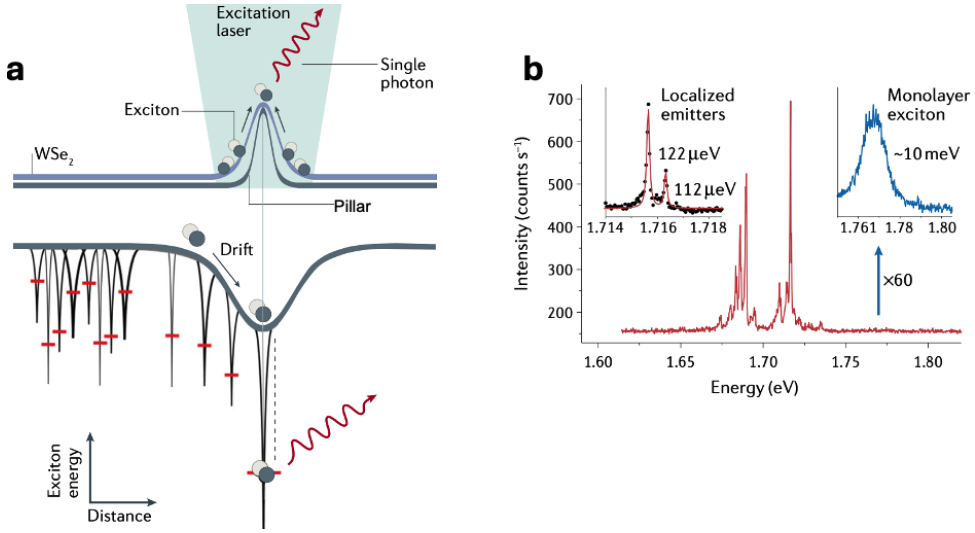

Figure 1.7: **Single–photon emission in strained WSe_2 monolayers.** (a) Schematic description of the phenomenon: localized interband states funnel one by one towards lower energy (i.e. high strain) sites, eventually recombining and emitting identical photons one by one. (b) Spectral signature of SPE in WSe_2 monolayers. The intensity and FWHM of localized emitters are compared with the ones of to the neutral exciton peak. Taken from [53].

1.3.4. Nanobubbles as a strain source for WSe_2 monolayer-based Single Photon Emission

Strain can be introduced in WSe_2 monolayers using several approaches. Nanopillar substrates are nanostructured supports that induce localized tensile strain in WSe_2 monolayers by forcing out-of-plane deformation when the monolayer is transferred on top, allowing deterministic positioning of emitters and compatibility with photonic integration. However, fabrication complexity and mechanical damage may limit their yield [41].
Alternatively, contaminant nanobubbles underneath the WSe_2 monolayer can be deliberately formed by annealing [16], producing strong local strain fields with relatively simple fabrication, as it was done for this work. Nanobubbles can generate high confinement po-

tentials, and various strain ranges can be obtained. As outlined in Section 3.2, the strain distribution within blisters depends sensitively on the adhesion at the substrate interface, enabling modulation of the optical response of nanobubbles via substrate selection. Their stochastic formation and limited spatial control constitute a significant limitation for scalable device integration. Nevertheless, a new approach to deterministically define bubble nucleation sites via laser writing is discussed in Section 3.3.

More specifically, the samples investigated in this work consist of WSe_2 monolayers containing contaminant-induced bubbles, stacked on multilayer MoS_2 substrates (1–5 layers). As represented in Figure 1.8, the multilayer MoS_2 is primarily employed to induce photoluminescence quenching in the unstrained regions of WSe_2 that are in direct contact with the substrate, owing to the type-II band alignment discussed in Section 1.1.2. This configuration enables selective probing of the strained sites via PL measurements. Additionally, MoS_2 is chosen as a substrate due to its layered nature: by controlling the number of MoS_2 layers it is possible to tune the adhesion between the substrate and the monolayer, and thus the strain induced within the bubbles, as discussed in Section 3.2 [4, 46].

The substrate thickness must be limited, as the tip-enhanced characterization setup described in Section 2.3.3 employs bottom illumination, with the laser incident from below the sample. Therefore, the substrate needs to be sufficiently transparent to ensure efficient optical excitation and signal collection.

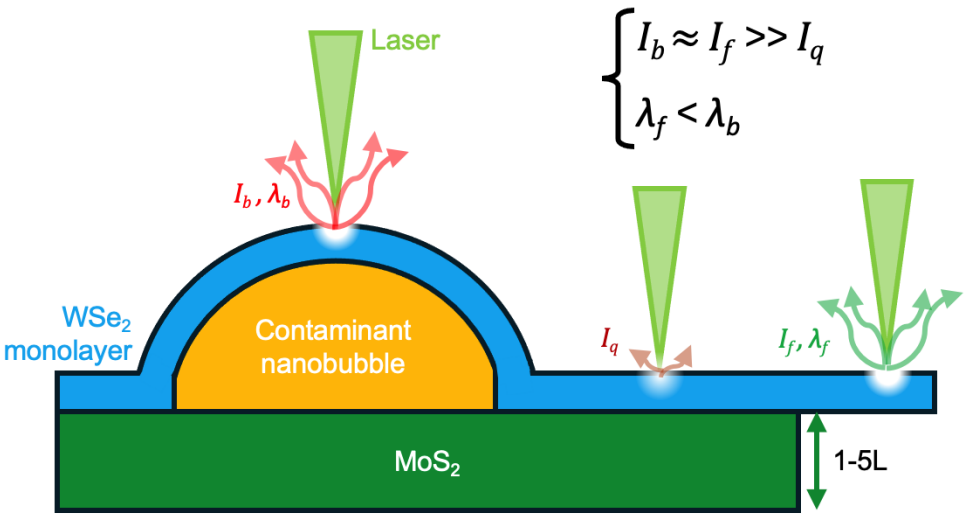

Figure 1.8: **Backscattered light in nanobubble-induced strain in WSe_2/MoS_2 stacks.** Free areas of WSe_2 monolayers have high intensity emission at 1.65 eV (I_f, λ_f), while within the bubble the monolayer is strained, thus has PL emission has similar intensity but at lower energies (i.e. higher wavelength). Where the WSe_2 is in direct contact with the MoS_2 substrate, type-II alignment of the band structure is obtained, thus the PL emission is quenched.

1.3.5. Open challenges and perspectives

For WSe_2 single-photon sources to be implemented in quantum computing applications, the physical mechanism underlying SPE in WSe_2 monolayers must be fully understood, which has not yet been achieved.
The aim of this work is to better understand the physical mechanism responsible for SPE in WSe_2. In particular, the hypothesis that SPE in strained WSe_2 monolayers originates from enhanced radiative recombination enabled by strain-induced hybridization between dark excitons and defect-related states is being investigated, as described in Section 1.2.2 [23, 31].

To test this hypothesis, photoluminescence (PL) measurements were performed on WSe_2 monolayers exhibiting nanobubble-induced strain (Section 1.3.4). The samples were cooled to cryogenic temperatures in order to investigate the PL evolution of strained WSe_2 monolayer down to temperatures close to the SPE onset using the setup described in Section 2.3.2. The local strain distribution was analyzed through tip-enhanced photoluminescence (TEPL) mapping, which provides PL spectra with nanometer scale resolution. From the local PL redshift measured on each bubble, the corresponding strain level was estimated. TEPL measurements were carried out according to the methods described in Section 2.3.3. This approach allows identification of the strain range associated with SPE.
In addition, this work examines whether the desired strain range can be controlled in advance by tuning the substrate thickness, as discussed in Section 3.2.

The long-term objective for the development of WSe_2-based single-photon sources is the implementation of strained WSe_2 monolayers as a scalable platform for single-photon sources [53]. Within this framework, strategies for the deterministic positioning of strain sites, and thus of emitters, are discussed in Section 3.3. Nanopillar-based approaches already enable deterministic placement of strain sources [41], but they involve more complex fabrication processes and, to date, there is no experimental evidence that the strain induced by nanopillars can be tuned by varying the substrate thickness, as demonstrated here for nanobubble-induced strain in Section 3.2.

2 | Materials and methods: Fabrication and Characterization of investigated devices

Following the introduction of the target sample structure in Chapter 1, this chapter describes the fabrication procedures employed, including the exfoliation of WSe_2 monolayers and MoS_2 multilayers, and the transfer of the former onto the latter.
This chapter also describes the experimental techniques used to acquire the relevant measurements. At first it focuses on Atomic Force Microscopy, which provides direct information on the nanobubble morphology, enabling quantitative analysis of their size and shape, and allows local variations in substrate thickness to be assessed. Finally introduces optical spectroscopy techniques, which are used to investigate the emission spectra of the samples as a function of temperature and excitation conditions, determine the thickness of the MoS_2 substrate and characterize the bubbles with PL below the diffraction limit.

2.1. Fabrication protocol

Several preparation procedures were explored during the development of the fabrication process; however, only two protocols produced reliable and reproducible results. These two protocols differ only in a single fabrication step, namely the method used to isolate the MoS_2 flake on the glass substrate.

2.1.1. Exfoliation on PDMS

Mechanical exfoliation is a widely used method to isolate two-dimensional materials down to the monolayer limit [40]. This approach is possible because the individual layers in layered crystals are held together by weak van der Waals interactions, which can be overcome by applying mechanical stress [35]. As a result, single layers or few-layer flakes

can be separated from the bulk material.

In this work, WSe_2 monolayers and MoS_2 flakes ,monolayer or multilayer, were exfoliated directly from the bulk material, provided by HQ Graphene. This can be done using both a dedicated exfoliation tape, namely Nitto tape ELP BT-150E-K or a standard adhesive tape. The latter is stable at higher temperatures, feature which can be useful as explained in Section 2.1.2, despite resulting in a higher level of surface contamination. After exfoliation, the flakes were transferred onto a polydimethylsiloxane (PDMS) substrate by simply applying the tape to the PDMS stamp and peeling it off subsequently. X4 PDMS from Gel–Pak was used, a polymer commonly employed as a support for 2D-material transfer due to its optical transparency, mechanical flexibility, and weak adhesion to exfoliated flakes. These properties make X4 PDMS suitable for both optical inspection and subsequent transfer steps. The flakes deposited on the PDMS substrates were then inspected under an optical microscope to identify flakes with very low optical contrast with respect to the substrate, as shown in Figure 2.1-a,b. Such low,but still visible, contrast is indicative of either WSe_2 monolayers or thin MoS_2 multilayers [40].

The presence of WSe_2 monolayers was confirmed by photoluminescence spectroscopy, as discussed in Sections 1.1.3 and 2.3.1. On the other hand, since part of the work focused on studying the dependency of nanobubbles optical properties on the substrate thickness, for MoS_2 flakes the observation of very low optical contrast was sufficient to deduce a small number of layers. The exact number of layers was determined, as discussed in Section 3.1, in a second moment, after the flake was transferred on the glass substrate, by combining the experimental techniques introduced in Sections 1.1.3 and 2.2.

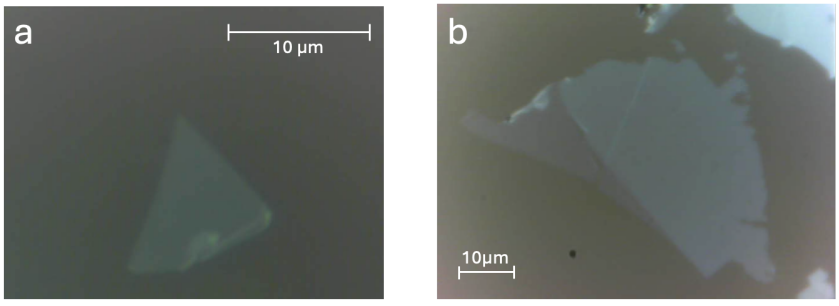

Figure 2.1: **Optical microscope picture of TMDs flakes on PMDS.** (a) Shows how low is the contrast of a WSe_2 monolayer with respect to the PDMS substrate. (b) A thin MoS_2 flake having two regions with different contrast, thus different thicknesses: one is a monolayer and one a bilayer, according to the analysis discussed in Section 3.1.

2.1.2. Exfoliation of MoS_2 on glass substrate

As discussed in Section 2.3.3, to be characterized with tip-enhanced methods, the stack has to be placed onto a transparent glass substrate, since the excitation laser comes from the bottom in the setup used.
While exfoliation of WSe_2 monolayers was only done on PDMS, MoS_2 multilayer flakes can instead be exfoliated directly onto a squared 0.17 mm thick glass coverslip by Fisherbrand. This approach allows one fabrication step to be skipped, as it avoids the need to transfer the MoS_2 flake onto glass prior to stacking the WSe_2 monolayer on top.

The process involves exfoliating MoS_2 onto an adhesive tape and then bringing the tape into contact with a clean glass coverslip placed on a hot plate at 120°C for two minutes. The tape must therefore be thermally stable and suitable for elevated temperatures, as demonstrated by common scotch tape. After heating, the tape with the attached coverslip is removed from the hot plate and allowed to cool to room temperature. The tape is then peeled off, leaving MoS_2 flakes on the glass surface. This protocol was selected after extensive testing because it provides a high flake yield while minimizing contamination from the adhesive. The coverslip is subsequently inspected under an optical microscope to identify flakes of interest as mentioned in Section 2.1.1.

2.1.3. Dry transfer in a motorized system

To obtain the target sample, at least one transfer step is required to place the flake of interest onto the substrate, two transfer steps are necessary when the MoS_2 flake is exfoliated on PDMS.
The transfer process is performed using a dedicated fully motorized system, namely HQ2D MOT by HQ Graphene (Fig. 2.2), which allows accurate alignment and controlled contact between the flakes with micron-scale precision. The entire setup operates inside a glovebox under a controlled nitrogen environment to minimize contamination and degradation of the materials, as shown in Figure 2.2-a.

During the transfer, the substrate is put on a motorized stage, while the PDMS stamp carrying the flake to be transferred is placed on a transparent mask positioned above the stage and facing downward, towards the sample. An optical objective is aligned above the mask, enabling real-time visual monitoring of the alignment and transfer process.
The system is remotely controlled, with the stage capable of moving only in the z direction (Figure 2.2-c, 3), while the transparent mask can move in the x–y plane and can be rotated around all the three axes (Fig. 2.2-c, 2). The objective is instead capable of motion along the x, y, and z directions, so that the focus can be adjusted (Fig. 2.2-c, 1). The

stage is also equipped with a heating system to allow temperature control during transfer (Fig. 2.2-c, 4), and a vacuum pump is used to fix the sample to the stage throughout the process (Fig. 2.2-c, 5).

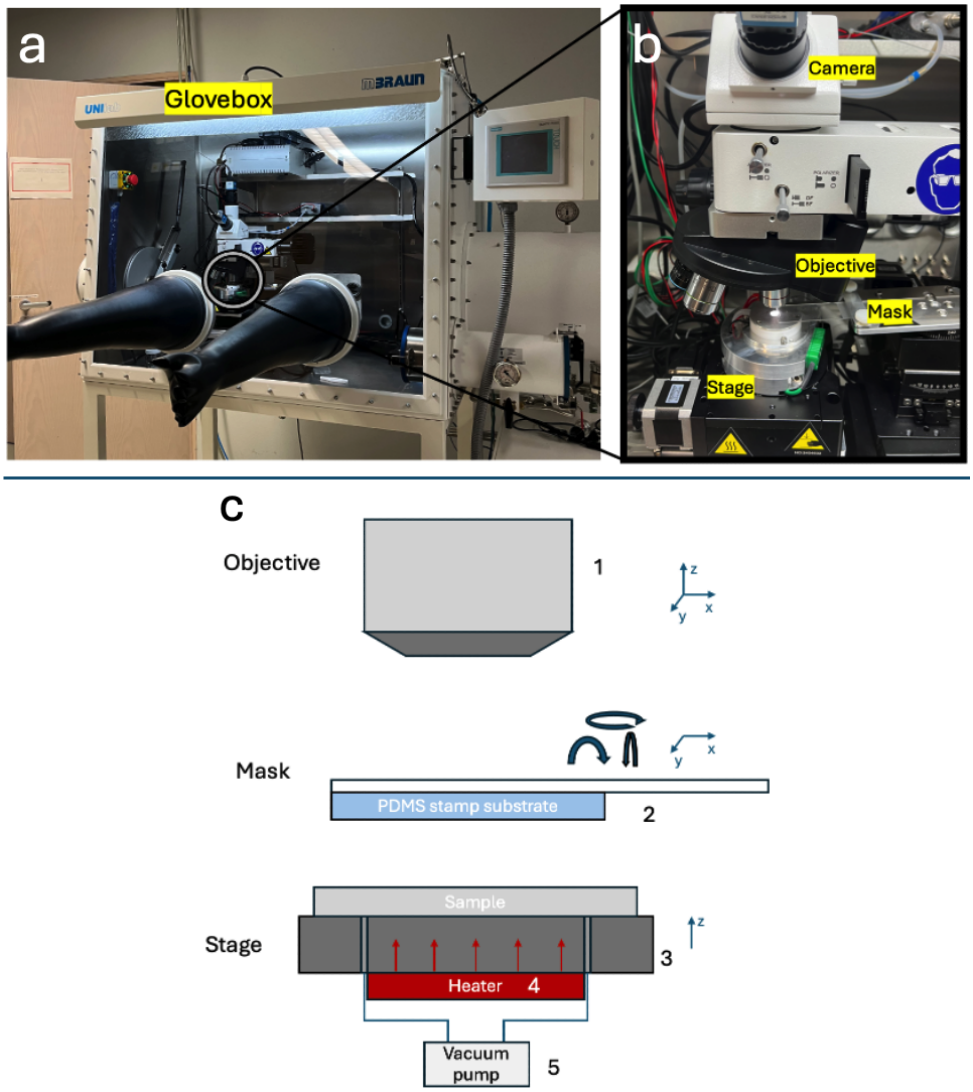

Figure 2.2: **HQ2D MOT by HQ Graphene transfer system and its operating conditions.** (a,b) Picture of the setup inside the glovebox, in a N_2 environment. (c) Schematic representation of the transfer setup components and their degrees of freedom. Here the objective (1), mask (2), stage (3) heater (4) and the vacuum pump (5) are shown.

The mask is slowly lowered toward the sample until the flake on the PDMS stamp comes into contact with the substrate. During this step, the stage temperature is typically increased to 60–70 °C in order to promote adhesion between the flake and the substrate. The mask is then gradually lifted to detach the PDMS stamp while releasing the flake in

question and avoiding its damage. Once the WSe_2 monolayer is successfully transferred onto the MoS_2 substrate as in Figure 2.3, the transfer step of the protocol is completed.

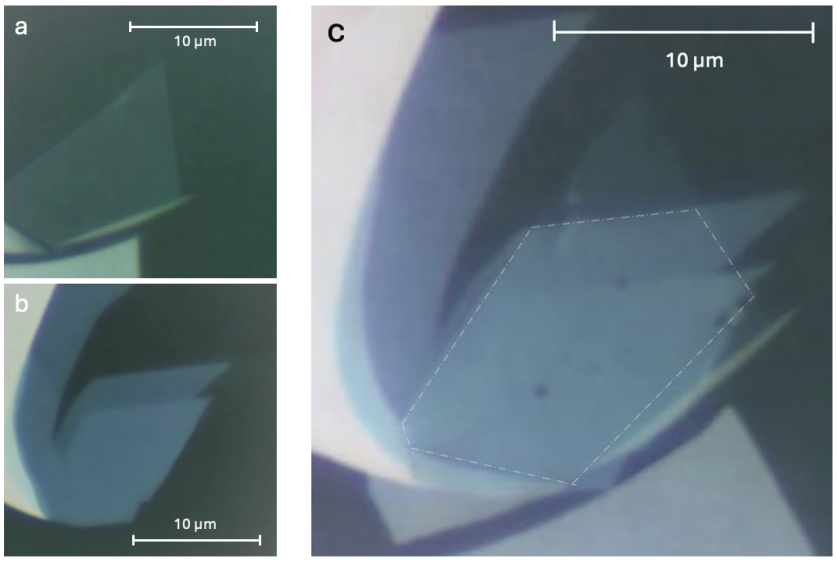

Figure 2.3: **Stack of aWSe_2 on a MoS_2 substrate on glass and its original flakes.** An optical microscope image of a WSe_2 monolayer on PDMS (a) and of a MoS_2 thin flake on glass (b). After the transfer, a change in contrast is induced within the overlapping area of the two flakes (c).

To promote the formation of nanobubbles, an annealing step is performed after the transfer. The sample is heated at approximately 200 °C for about 12 h. This process is carried out on the heated stage of the motorized transfer system under an oxygen-free atmosphere, in order to prevent high-temperature oxidation of the involved TMDs.
The high temperature increases the mobility of contaminant particles trapped between the two layers. These particles coalesce and form nanobubbles, which elastically strain the WSe_2 monolayer [16].

2.2. Atomic Force Microscopy

Atomic Force Microscopy (AFM) is an experimental technique that allows the investigation of surface morphology and local physical properties with sub nanometer-scale resolution.
It is of interest in this work because it enables the investigation of nanobubble dimensions, the determination of the number of layers in the MoS_2 substrate, and is involved in tip-enhanced spectroscopy methods, which are discussed in more detail in Section 2.3.3.
The technique is based on the interaction forces between a sharp tip and the sample

surface, which are monitored while the tip is scanned across the surface.

The whole AFM setup consists of the sharp tip mounted on a flexible cantilever, a piezoelectric scanner for precise positioning and an optical detection system, typically based on a laser beam reflected onto a position-sensitive photodetector, as shown in Figure 2.4-a. As the tip scans the sample surface, tip–sample interaction forces cause a change in deflection or oscillation of the cantilever, which is measured and used to reconstruct surface topography.

In this work, AFM measurements were performed using a Nanowizard 3 setup, by JPK Instruments, shown in Figure 2.4-b. In this setup, the tip is mounted on a movable piezoelectric scan head, while the sample remains fixed on a stationary stage below. An optical microscope coupled to a camera allows alignment between the tip and the sample. A computer controls and monitors the entire scanning process. To carry out the experiments, AFM tips by Olympus were used, having a resonance frequency of 70 kHz and a spring constant of 1.7 N/m.

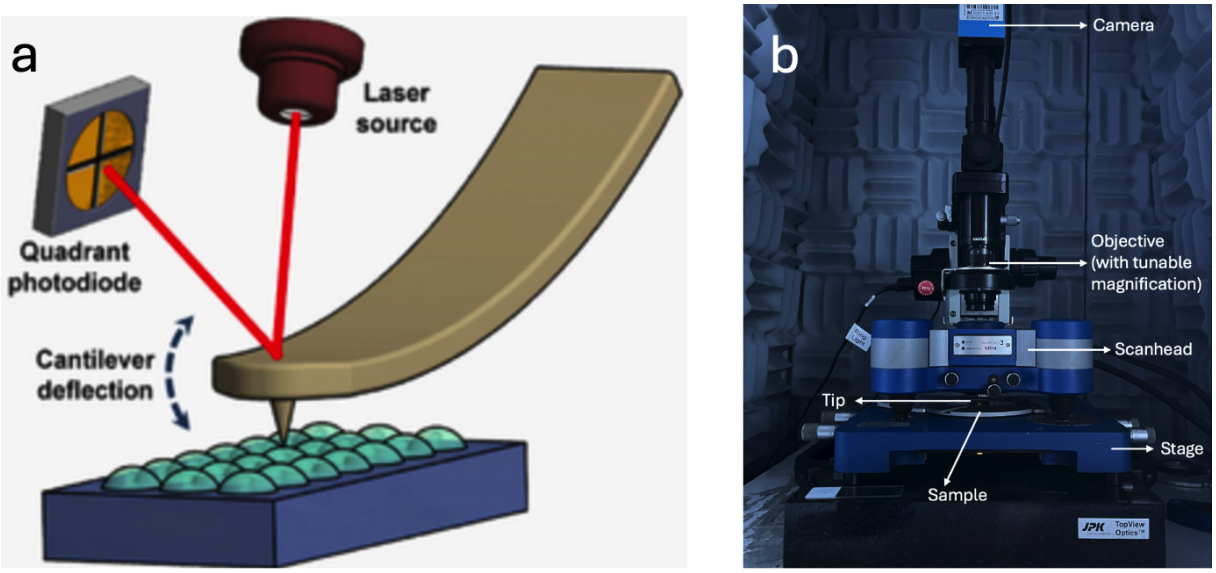

Figure 2.4: **Representation of an AFM setup.** (a) Schematic representation of an AFM setup: a laser beam is pointed on the cantilever, and its reflection is subsequently measured by a photodiode. Taken from [3]. (b) AFM setup employed in this work, namely Nanowizard 3 by JPK Instruments. Here is shown the tip fixed on the movable scanhead, and placed on top of the stage where the sample is put. An objective with tunable magnification is aligned to the tip and the sample, transmitting to a camera to keep the measurement monitored.

The interaction between the tip and the sample is often described using the Lennard–Jones

potential, which provides a simple model for the balance between attractive and repulsive forces at short distances. Although simplified, this model captures the essential physics of van der Waals attraction at larger distances and Pauli repulsion at very short distances, making it suitable for a qualitative description of AFM force regimes [22]. As shown in Figure 2.5, the Lennard Jones potential can give an attraction force or a repulsive one depending on the distance between the tip and the sample.

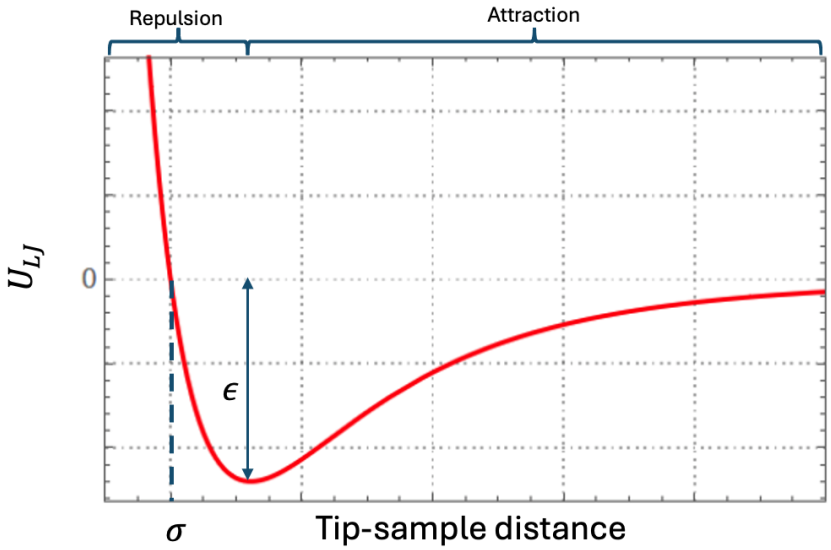

Figure 2.5: **Lennard–Jones potential plotted.** ε quantifies the strength of the interaction between the AFM tip and the 2D material surface, while σ represents the characteristic tip–surface separation at which the interaction potential is zero, setting the effective interaction length scale. Since $F(r) = -\frac{dV(r)}{dr}$, there's a repulsive regime before the minimum and an attractive one after it [22].

Depending on the distance between sample and tip, AFM can operate in three different modes:

- **Contact mode**: the tip is kept in contact with the sample (Fig. 2.6-a-1), being constantly in the repulsive regime of the Lennard-Jones potential. While scanning feedback loop continuously adjusts the height of the tip through the piezoelectric scanner, in order to keep constant the deflection of the cantilever, and thus the force acting on it [43].
- **Tapping mode**: the cantilever is driven to oscillate near its resonance frequency while the tip remains slightly above the sample surface, ranging both in the repulsive and the attractive regimes (Fig. 2.6-a-2) [43]. Tip–sample interactions modify the oscillation amplitude, and a feedback loop acts on the piezoelectric scanhead to

maintain a constant oscillation amplitude at a predefined setpoint, as shown in Figure 2.6-b.

- **Noncontact mode**: the tip remains at a fixed distance from the sample surface (Fig. 2.6-a-3), remaining in the attractive regime [43]. Also in this case, the piezoelectric scanner acts to continuously keep constant the force acting on the tip.

In this work, all AFM measurements were performed in tapping mode, where the topographic information is obtained from the vertical displacement z of the piezoelectric scanhead required to compensate for changes in the tip–sample interaction during scanning. The height maps presented in this work therefore directly correspond to the z-motion of the scanhead necessary to keep the cantilever oscillation amplitude constant.
This mode has two main advantages, which are high lateral resolution and less damage to the samples [43].

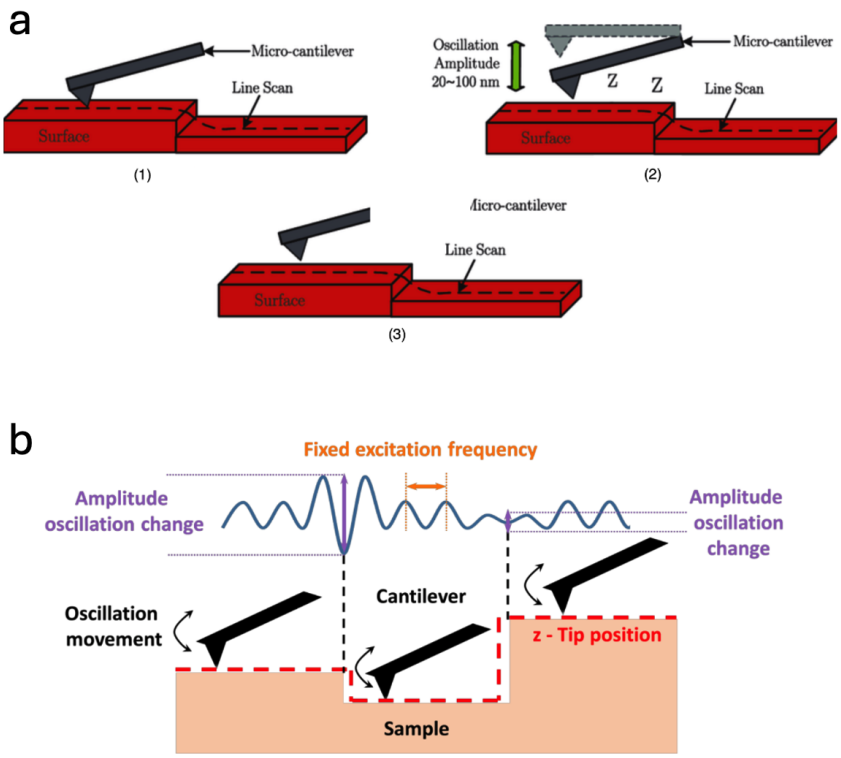

Figure 2.6: **AFM scanning modes.** (a) Representation of the three AFM modes: contact mode (1), tapping mode (2) and noncontact mode (3). Taken from [43]. (b) Tapping mode with amplitude modulation mechanism: when a difference in the cantilever oscillation amplitude is detected by the photodiode, the stage is adjusted to return to the set conditions. Taken from [21].

With this technique, Angstrom-scale resolution of the sample morphology is obtained.

The AFM technique is not limited to acquiring spatial maps of the sample surface, but is also implemented in tip-enhanced spectroscopy, as discussed in Section 2.3.3. Since the tip–sample distance is a critical parameter for tip enhancement and direct contact must be avoided, the AFM operates in shear-force mode in this configuration [38, 50]. In shear-force mode, the AFM tip oscillates laterally, parallel to the sample surface. Near-field interactions damp the oscillation amplitude or shift the resonance. This change provides the feedback signal to maintain a constant tip–sample distance without physical contact.

2.3. Optical spectroscopy techniques

This work studies the optical properties of TMDC heterostructures using optical spectroscopy techniques. While room-temperature photoluminescence and Raman spectroscopy provide basic characterization, a full analysis of the localized emitters introduced in Chapter 1 requires more advanced approaches. Resolving strain-induced spectral variations within individual nanobubbles requires sub-diffraction spatial resolution, which can be achieved with tip-enhanced methods. In addition, measurements at cryogenic temperatures are needed to clearly resolve excitonic features, requiring the integration of a cryostat into the PL setup.
Since the physical mechanisms were discussed in Chapter 1, this section focuses on the experimental setups used for the spectroscopic measurements.

2.3.1. Equipment for confocal methods at room temperature

Photoluminescence and Raman spectroscopy, the two spectroscopic techniques used in this work, can be performed within the same experimental setup. Two different systems were employed: a commercial setup, the XploRA Plus by Horiba, used for room-temperature measurements, and a custom-built setup for spectroscopy at cryogenic temperatures. This section focuses on the commercial XploRA system used for room-temperature spectroscopy, while the instrumentation used to for spectroscopy techniques is described in Section 2.3.2.

The XploRA setup (Figure 2.7-a) consists of a motorized stage on which the sample is mounted, with independent motion along the x, y, and z directions. An optical objective is positioned above the stage and can be coupled either to a camera or to a spectrometer, depending on the requirement. The system includes three different excitation laser sources having wavelength: 532 nm, 638 nm, and 765 nm. As shown in Figure 2.7-b, the laser beam is fiber-coupled and transmitted to a collimating lens (L_1). The collimated beam passes then through a filter (F_1) which can be changed depending on the excitation power

required (See Table 2.1). The collimated and filtered beam is then reflected on a beam splitter (BS), which reflects part of it towards the objective. The lens in the objective (L_2) focuses the beam on the sample, causing light absorption and subsequent emission or Raman scattering in the sample.
The backscattered light is collected by the objective and collimated by its lens towards the beam splitter, which transmits part of the beam to a new filter and lens system (F_2, L_3). The latter one focuses the beam, which is fiber-coupled to a spectrometer. Inside the spectrometer, the incoming light is dispersed by a diffraction grating and detected by a CCD camera. Due to this dispersion, each pixel along the horizontal axis of the CCD corresponds to a specific wavelength, so by recording the intensity as a function of it a portion of the emitted spectrum is obtained.
The setup allows the selection of different diffraction gratings with groove densities of 600, 1200, 1800, and 2400 gr/mm, each one providing a different spectral resolution. The orientation of each grating can be adjusted to access different wavelength intervals.

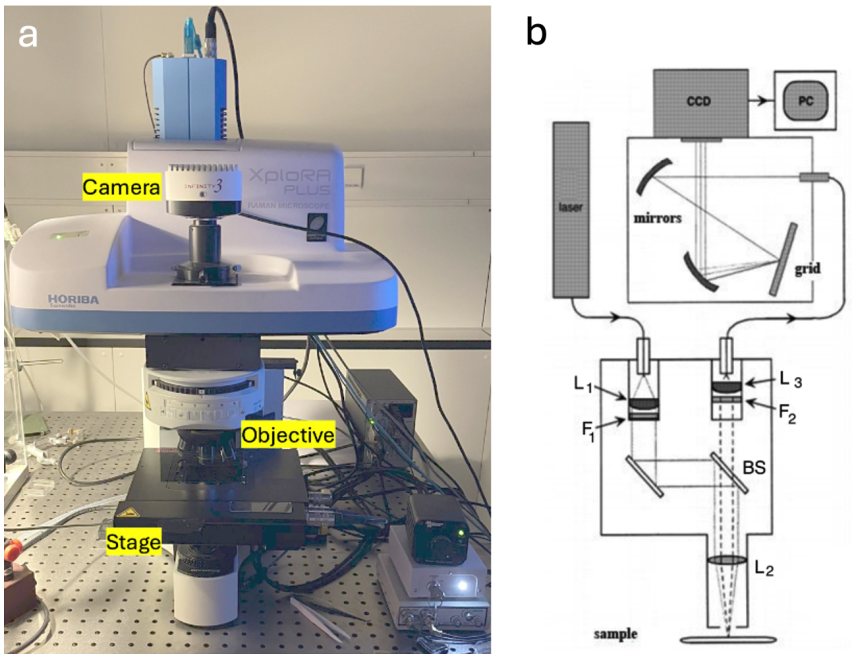

Figure 2.7: **XploRA Plus setup by Horiba.** (a) The components accessible by the user in the setup are shown in this picture: the stage onto which the sample is put, the objective to focus the beam and collect the emitted light, the camera to image the sample. (b) Schematic representation of the experimental setup, taken from [28]. Both the excitation laser beam and the backscattered light are guided through a system of lenses and filters. Finally, a diffraction grating disperses the light into its spectral components and directs them toward a CCD detector.

PL and Raman maps are acquired by scanning the region of interest with the objective while translating the sample stage. The pixel size of the map, corresponding to the spatial step between consecutive spectra, can be defined by the user. The acquisition time for each spectrum can also be independently set.

By changing filters F_1 and F_2 in Figure 2.7 and the laser source, the laser power delivered to the sample can also be adjusted, as shown in Table 2.1:

XploRA laser power (mW)

Filter	**Laser wavelength**		
	532 nm	**638 nm**	**785 nm**
0.1%	0.008	0.008	0.086
1%	0.160	0.095	0.85
10%	1.60	0.90	5.70
25%	3.70	2.40	13.0
50%	6.75	4.90	24.0
100%	11.7	9.20	40.0

Table 2.1: **Possible laser power in the XploRA setup**. The different values were measured using a power meter for different filters and laser wavelengths.

Both the laser wavelength and the total laser power are key parameters for deterministic nanobubble patterning discussed in Section 3.3.

2.3.2. Setup for confocal spectroscopy at cryogenic temperatures

As discussed in Section 1.2.1, reducing the temperature of strained WSe_2 monolayers is crucial for investigating excitonic states and localized emitters in two-dimensional materials, as thermal broadening is suppressed and strain-induced modifications of the excitonic states become more clearly observable.

The optical setup used for low-temperature measurements is integrated in a custom-built setup described in Figure 2.8, into which a cryostat for low temperature measurements can be implemented.

The laser source with tunable frequency, C-wave by Hübner Photonics, provides a contin-

uous wave excitation beam. A set of steering mirrors (M1–M3) directs the beam toward the main optical table while preserving beam alignment. A continuous neutral density (ND) filter wheel allows fine control of the laser power before it enters the rest of the setup. The beam then passes through a beam expander (BE) to control the beam diameter by spatially filtering it. Additional mirrors (M4–M7) guide the beam into the microscope coupling section.
Inside the central block, Mirrors M8–M10 form a folded optical path that ensures compactness and proper beam alignment, before a beam splitter (BS) separates the excitation and collection paths. The excitation beam (in green) is sent toward the microscope, where a Mitutoyo MY100x-806 objective (N.A.=0.7) focuses the beam onto the sample, while the back-scattered signal (in red) is redirected toward the spectrometer. This is done as mirrors M11–M16 steer the beam through a tunable filter and a tweaker plate, which allow fine wavelength selection and polarization or phase adjustment. A lens is used to focus the beam before it gets into the spectrometer.

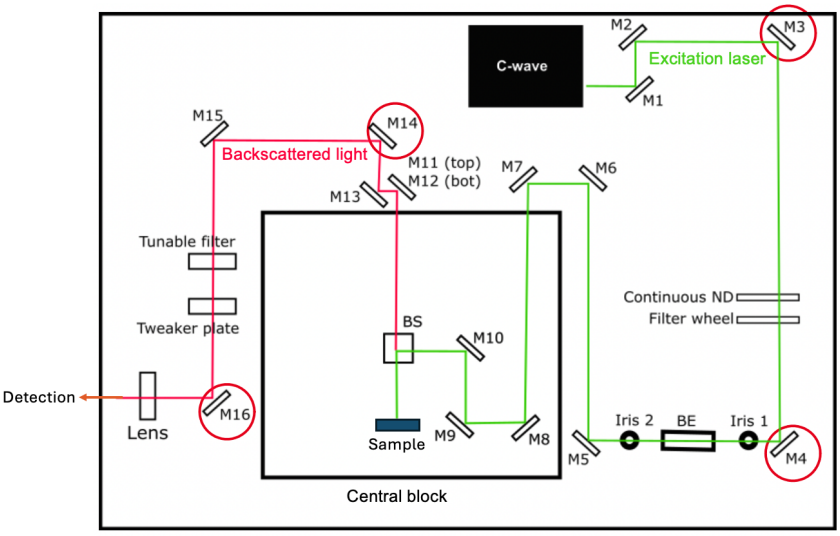

Figure 2.8: **Custom-built setup for confocal spectroscopy.** The excitation laser beam (in green) is guided to the sample through a system of mirrors and filters, and focused onto the sample. The backscattered light beam (in red) is transmitted to a spectrometer through another system of mirrors and filters. The mirrors highlighted with a red circle are the ones movable by the user.

The sample is placed onto a movable stage, which can be equipped with a cryostat to perform photoluminescence spectroscopy at cryogenic temperatures.
To achieve cryogenic cooling, the sample is placed inside a LakeShore SuperTran ST-500

continuous-flow cryostat (Figure 2.9-a) and mounted on a metallic sample holder thermally anchored to a gold-platted copper heat exchanger, as shown in Figure 2.9-b. Liquid helium is delivered to the cryostat through a high-efficiency, flexible transfer line, insulated with a vacuum jacket, which supplies the cryogen to the heat exchanger. The entire cryostat is maintained under high-vacuum conditions, achieved using a pumping station composed of an MVP015-2 rough pump and a HiPace 80 turbomolecular pump by Pfeiffer Vacuum. The vacuum environment serves two main purposes: it minimizes thermal heat transfer through gas conduction, improving cooling efficiency, and it prevents condensation or ice formation on the sample surface at low temperatures. In these conditions, the sample temperature can reach approximately 4K.
A heater is also integrated into the cryostat, enabling controlled and stable temperature increases. This allows the optical properties of the sample to be systematically investigated in a temperature range in between 4 and 475 K [51]. A temperature sensor mounted on the heat exchanger is connected to a temperature controller, which continuously operates a feedback loop to maintain the temperature at the set value by regulating the heater. The sample is placed inside a radiation shield that intercepts room temperature radiation. An optical window at the top of the cryostat enables photoluminescence spectroscopy.

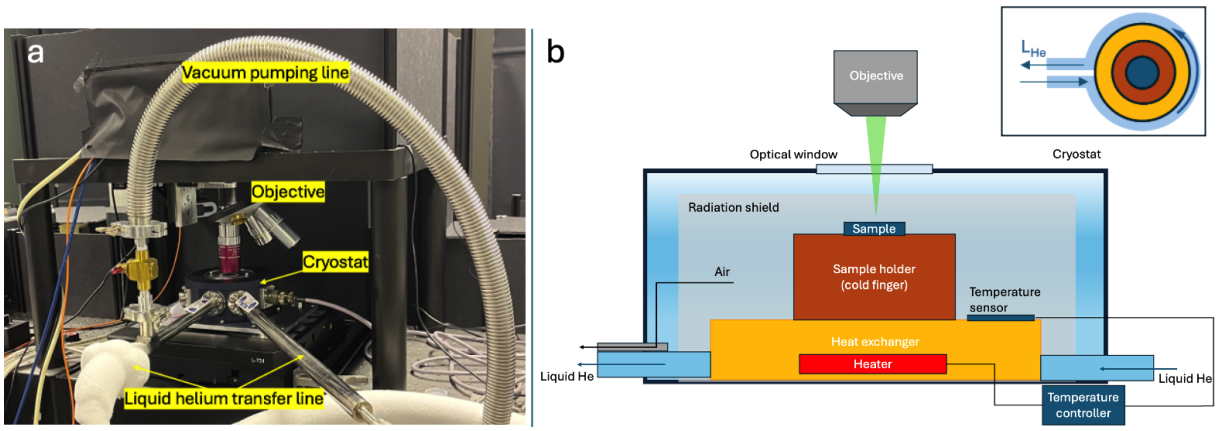

Figure 2.9: **Cryostat and main components for low temperatures spectroscopy**. (a) Cryostat mounted on the stage and connected to the vacuum pumping line and the liquid helium transfer line. (b) A schematic representation of the internal configuration of the cryostat is shown: the cold finger, thermally coupled with the heat exchanger, dissipates heat through direct contact with the helium transfer line. A radiation shield surrounds the cold finger and the sample to intercept the room temperature radiation. High vacuum is obtained through a duct connected to the pumping system. An optical window on top enables PL spectroscopy.

2.3.3. Tip-enhanced spectroscopy

Despite the high spatial resolution achievable with confocal spectroscopy described in Section 2.3.1, there exists a fundamental theoretical limit to optical resolution, known as the diffraction limit. Features with dimensions smaller than this limit cannot be spatially resolved using conventional far-field spectroscopy techniques, thus the best achievable lateral resolution is usually in the order of hundreds of nanometers when using visible light excitation lasers, as it was done in this work [9]. This limitation becomes particularly relevant when investigating nanoscale optical features, such as single photon emission hotspots [14]. To overcome this limitation, additional approaches are required, one of these is tip enhancemnet.

Tip-Enhanced Raman Spectroscopy (TERS) and Tip-Enhanced Photoluminescence (TEPL) are near-field optical techniques that overcome the diffraction limit of conventional far-field spectroscopy. Both methods rely on the strong electromagnetic field localized at the apex of a metallic tip to enhance the optical signal from a nanoscale region of the sample. This approach enables optical characterization with spatial resolution well below the diffraction limit, being a key tool for strain characterization of nanobubbles hosting Single Photon Emission, as it will be discussed in Section 4.1.
As schematically represented in Figure 2.10-a, tip-enhanced spectroscopy techniques combine a scanning probe with an optical microscope. A metallic tip is positioned a few nanometers above the sample surface, while the sample is illuminated by a focused laser beam and the scattered/emitted light is collected by the same objective. The key element is that the tip apex behaves as an optical nano-antenna: due to a localized surface plasmon resonance induced by the excitation laser on the tip, the electromagnetic field becomes strongly confined and enhanced in a nanoscale volume near the tip apex [38]. The effective spatial resolution is therefore not set by diffraction, but mainly by the tip radius and by the tip–sample gap. A sharper tip leads to a stronger confinement of the electromagnetic near-field, thereby reducing the effective interaction area. As a result, the lateral resolution achievable in tip-enhanced measurements is largely independent of the diffraction limit and is typically on the order of 10–30 nm [55]. The resolution difference between a confocal and a tip-enhanced spectroscopy can be visualized in Figure 2.10-b, where a TERS and a confocal Raman map performed onto the same graphene flake are compared [26].
In TERS, the scattered signal per unit area can be amplified up to 10^5 times [26]. The difference in signal intensity between confocal and tip-enhanced Raman spectroscopy is displayed in Figure 2.10-c, where the E_{2g} and A_{1g} peaks of MoS_2 are plotted for both methods.

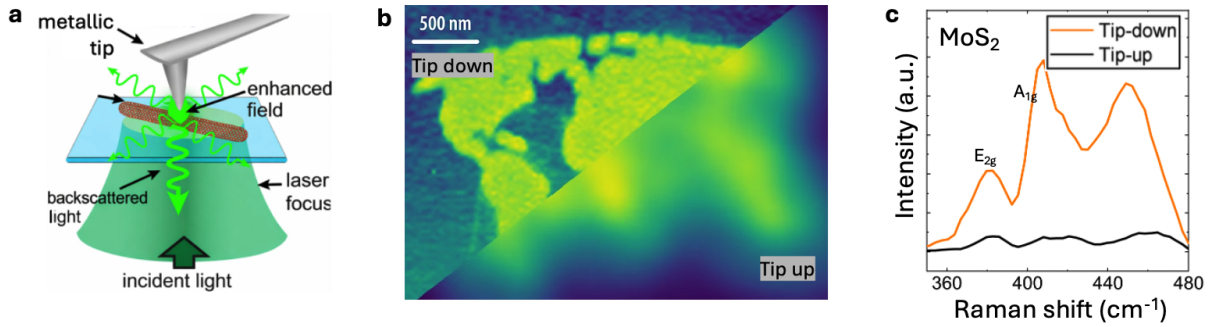

Figure 2.10: **Tip-enhancement in 2D materials.** (a) Schematic representation of the working principle of tip enhancement: the metallic tip amplifies locally the electromagnetic field due to surface plasmon resonance. Taken from [55]. (b) World map drawn onto a graphene sheet using a focused He ion beam, and imaged using both confocal (tip up) and tip-enhanced (tip down) Raman spectroscopy. Taken from [19]. (c) Tip enhancement of E_{2g} and A_{1g} Raman modes in MoS_2. Adapted from [26].

Different experimental geometries can be employed depending on the relative position of the laser beam, the objective lens, and the tip with respect to the sample, as shown in Figure 2.11: bottom illumination/collection (Fig. 2.11-a), top illumination/collection (Fig. 2.11-b), and side illumination/collection (Fig. 2.11-c) geometries can be used [7]. In each case, the goal is to efficiently excite the localized plasmon at the tip apex while maximizing the collection of the optical signal. The emitted signal is then collected through the objective and sent to an optical detector.

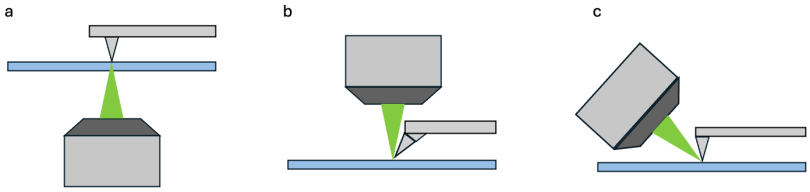

Figure 2.11: **Different architectures for Tip-Enhanced spectroscopy.** Here are shown bottom illumination/collection (a), top illumination/collection (b) and side illumination/collection (c) configurations.

In the experiments presented in this work, a bottom-illumination/collection geometry was used, with the laser beam focused onto the sample through a transparent substrate, while

the metallic tip approached the sample surface from above. This configuration allows stable tip operation and efficient optical access to the tip–sample junction, but requires optically transparent samples and substrates. For this reason, all samples analyzed in this work were fabricated on a glass substrate, namely 0.17 mm thick cover glasses by Fisherbrand, and the MoS_2 layers were kept as thin as possible in order to reduce optical absorption [38], as it was explained in Section 2.1.2.

More specifically, the Porto setup developed by FabNS was employed (Fig. 2.12-a): this system combines a confocal microscope with an AFM scanning head integrated above the optical path. As shown in Figure 2.12-b, the laser beam is focused onto the sample and the metallic tip using an inverted microscope equipped with an oil-immersion Nikon x60 MRD01605 objective with numerical aperture NA = 1.4, to increase definition and thus the local field at the tip. The light scattered from the sample is collected in back-scattering configuration and directed to the spectrometer. The AFM unit operates in shear-force non-contact mode, as discussed in Section 2.2, with a resonance frequency of approximately 32 kHz. The shear force AFM mode is crucial as it allows to keep a fixed tip-sample distance while scanning the sample surface. In the present configuration, excitation is provided by a laser with wavelength $\lambda = 632.8$ nm [38]. The AFM unit consists of two bonded piezoelectric actuators forming a tunning fork (Fig. 2.12-b), which independently control the motion along the z axis and in the x–y plane, and are mounted on the scan head body. The tunning fork electrodes are soldered to the tip, enabling oscillation detection and feedback control [26].

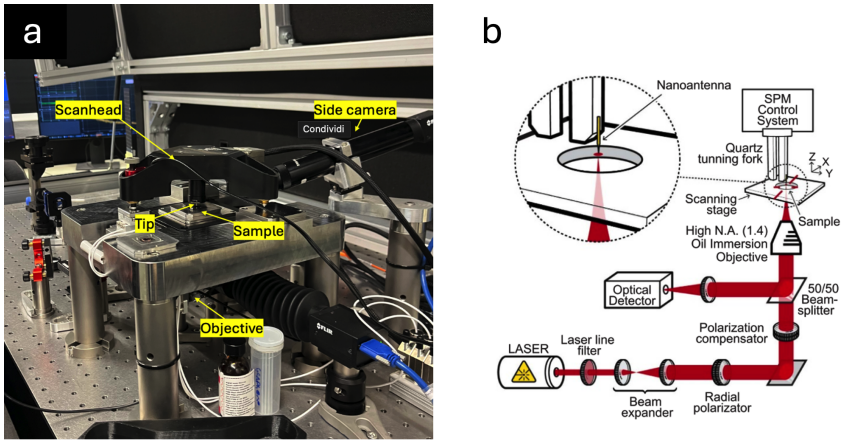

Figure 2.12: **Porto setup for tip-enhanced spectroscopy**. (a) Disposition of the components. (b) Schematic representation of PORTO tip-enhanced spectroscopy setup: the laser beam enters the microscope through a beam splitter and interacts with the sample and the tip. The enhanced signal is then backscattered and routed toward the spectrometer. Taken from [26].

More specifically, a plasmon-tunable tip pyramid (PTTP) by FabNS is attached to one prong of the tuning fork, and acts as both AFM probe and plasmonic antenna.
As shown in Figure 2.13, PTTPs are sharp tips featuring a gold pyramid at one end with flat plateau at the apex (Fig. 2.13-a). A nanopyramid is fabricated on this plateau and supports localized surface plasmon resonances, which enhance the optical signal originating from the substrate (Fig. 2.13-a).

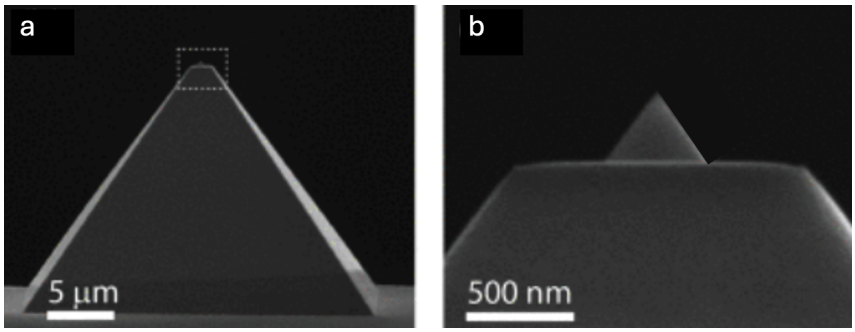

Figure 2.13: **SEM image of a PTTP tip, taken from [54]**. (a) Shows the whole pyramid body, while (b) shows in detail the plateau with the nanopyramid on top.

3 | Strain engineering of nanobubbles

For the TMDs stacks investigated in this work, the ability to anticipate the resulting optical behavior and spatial distribution of emitters based on the fabrication procedure is crucial for achieving controlled and reproducible sample configurations. This chapter focuses on two main themes related to the final sample morphological and optical properties. The first is the investigation of nanobubble strain as a function of the number of MoS_2 layers in the substrate, a plausible explanation of the observation will be provided as well. The second is the development of a fabrication protocol that enables deterministic nanobubble patterning in the final sample, a phenomenon that is not yet fully understood, but that may represent a step forward in the realization of strained WSe_2 monolayer-based Single Photon Emitters devices for practical applications.

3.1. Determination of the number of MoS_2 layers in the substrate through custom-built reference

To investigate how the properties of nanobubbles depend on substrate thickness, a reliable method to determine the number of MoS_2 layers in each sample is required.
This determination can be carried out using a combination of experimental techniques discussed in Chapters 1 and 2, namely AFM, photoluminescence, and Raman spectroscopy. These methods provide complementary information on thickness and layer number.

A reference MoS_2 sample was fabricated and characterized, providing an internal benchmark for the layer identification. To achieve an exhaustive dataset, the reference flake had to show various numbers of layers all at once, as shown in Figure 3.1-a.
After characterization by AFM (Fig. 3.1-b,c), photoluminescence (Fig. 3.1-d) and Raman spectroscopy (Fig. 3.1-g), the flake was found to contain regions with thicknesses of two, three, four and six layers. The layer number was determined by comparing the PL spectrum of the thinnest area (Fig. 3.1-e) with reference data reported by Mak et al. [34],

and by comparing the step heights extracted from AFM line profiles (Fig. 3.1-c) with the thickness of a monoatomic MoS_2 layer reported by Chhowalla et al.[11], namely of 0.7 nm approximately.

From the PL spectra reported in Fig. 3.1-e, it is evident that, in addition to the direct K–K transition peak at 1.87 eV, a second peak appears at lower energy, which is attributed to indirect Γ–Q recombination [34]. As shown in Figure 3.1-f, the indirect transition peak rapidly decreases both in intensity and energy position with the number of MoS_2 layers. From the characterization of the sample by Raman spectroscopy, the two most intense peaks detected are the A_{1g} mode at ∼405 cm^{-1}, and the E_{2g} mode at ∼385 cm^{-1}, both reported in Figure 3.1-h. A_{1g} is related to the out-of-plane vibration of sulfur atoms, while E_{2g} mode is related to the in-plane vibration of the single MoS_2 layer [29], as discussed in Section 1.1.3. As shown in Figures 3.1-h and 3.1-i, both the intensities and the relative distance in between these two peaks rise with the number of layers.

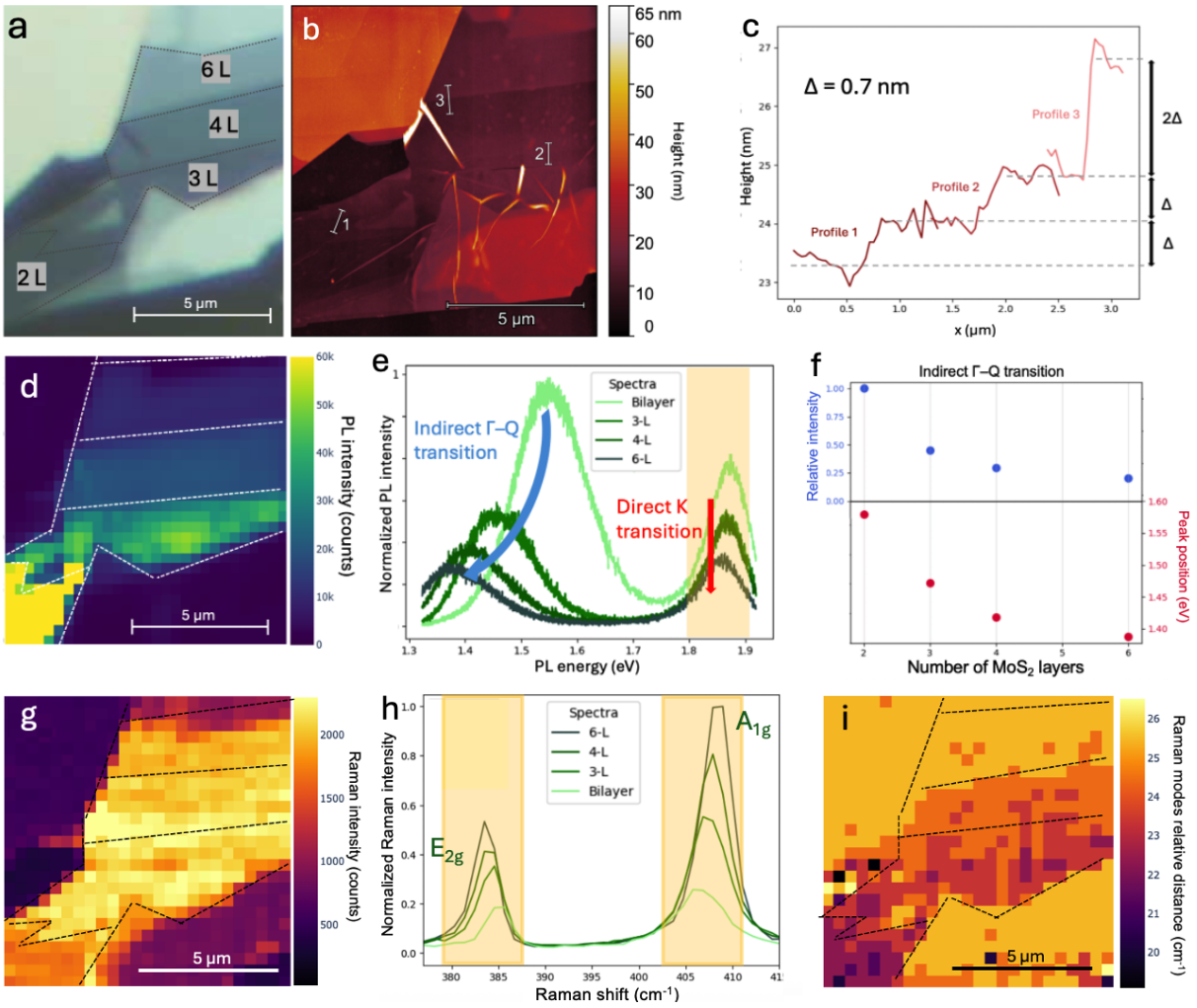

Figure 3.1: **Complete characterization of MoS_2 reference.** (a) Optical microscope image of the MoS_2 reference on glass, showing areas with different contrast and thus different thickness. (b) AFM map of the flake and investigation on the difference in thickness in between areas with different contrast (c). According to Chhowalla et al. [11], the step increase is of one layer for Profiles 1 and 2, and of two layers for Profile 3. (d) PL map of MoS_2 direct recombination peak and plot of PL emission for different thicknesses of the sample (e). Peaks related to both the indirect and direct recombination mechanism are visible, as well as their change in intensity and position (f). (g) Heatmap of A_{1g} and E_{2g} Raman peaks, plotted for different areas of the sample (h). The spectral distance between the two peaks grows within thicker areas (i).

As shown in Figure 3.1-e, the PL spectrum of MoS_2 bilayers can be easily distinguished, both for the peculiar position of the Γ–Q recombination peak at ∼1.6 eV and the higher peaks intensity with respect to thicker flakes. On the other hand, as discussed in Section 1.1.1, MoS_2 monolayers are direct band gap semiconductors, showing one main intense

peak at 1.87 eV, related to K–K direct recombination [34].
For these reasons, in this work the number of layers in samples with one- or two-layer-thick substrates was determined directly from photoluminescence spectroscopy, as shown in Figure 3.2.

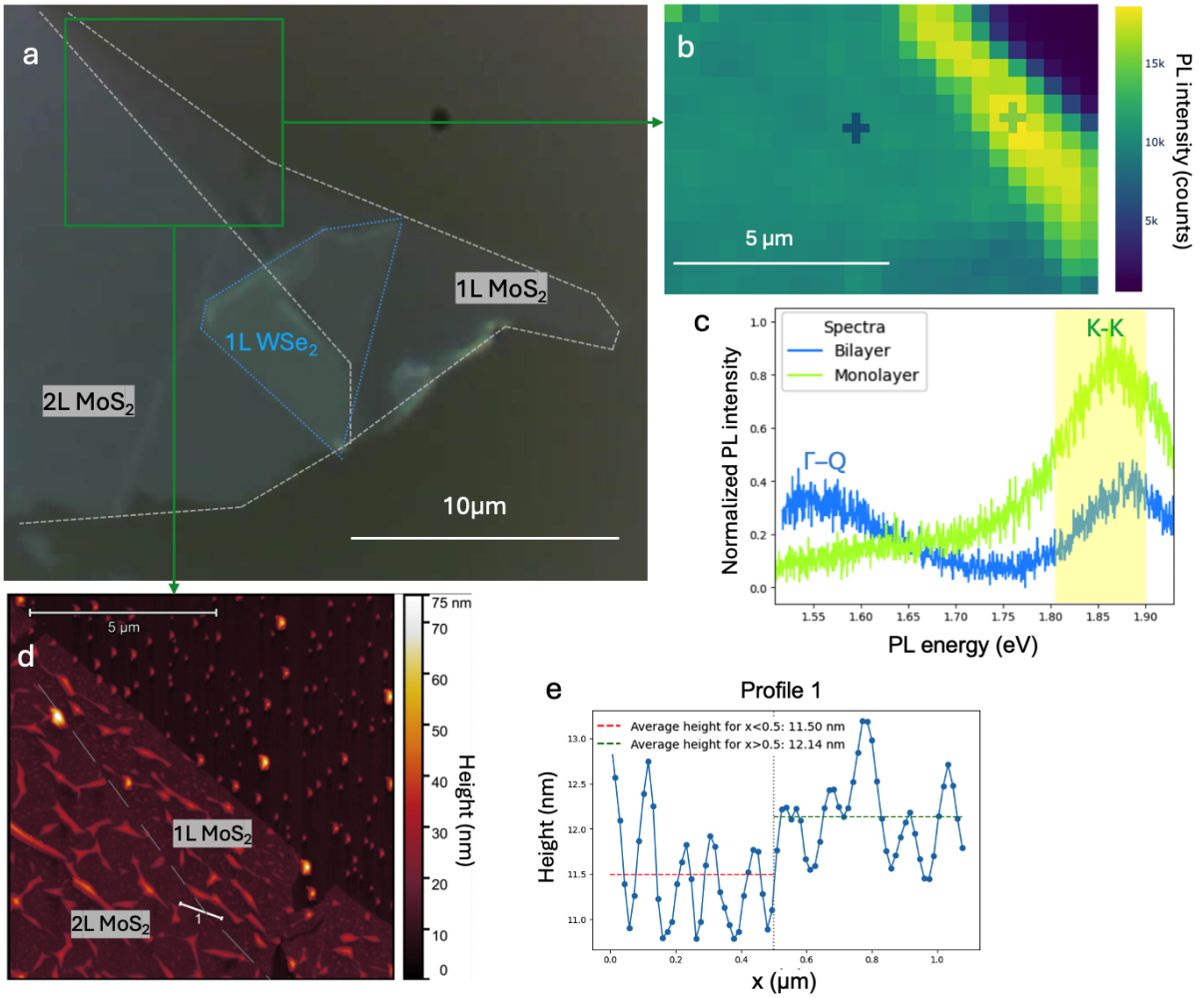

Figure 3.2: **Determination of the number of layers in the substrate using PL.** (a) Optical microscope image of the analyzed sample on glass. The sample shows areas having two different contrasts and thus thicknesses. (b) PL map of both MoS_2 thicknesses, the PL spectra for each area and the integration interval are reported in (c): according to Mak et al. [34], the MoS_2 flake is one and two layers thick. (d) AFM map performed within the analyzed area and the profile extracted in correspondence of the change in contrast (e) confirm that the change in thickness is of one layer only, as the increase in average height is of 0.64 nm [11].

For thicker MoS_2 substrates, the number of layers was instead determined by Raman spectroscopy, by comparing the measured spectra with reference data. In particular,

the spectral distance between the A_{1g} and E_{2g} modes was used as the main indicator of thickness. This separation was calculated for each region of uniform thickness in the analyzed samples and in the reference flake. The results are reported in Figure. 3.3.

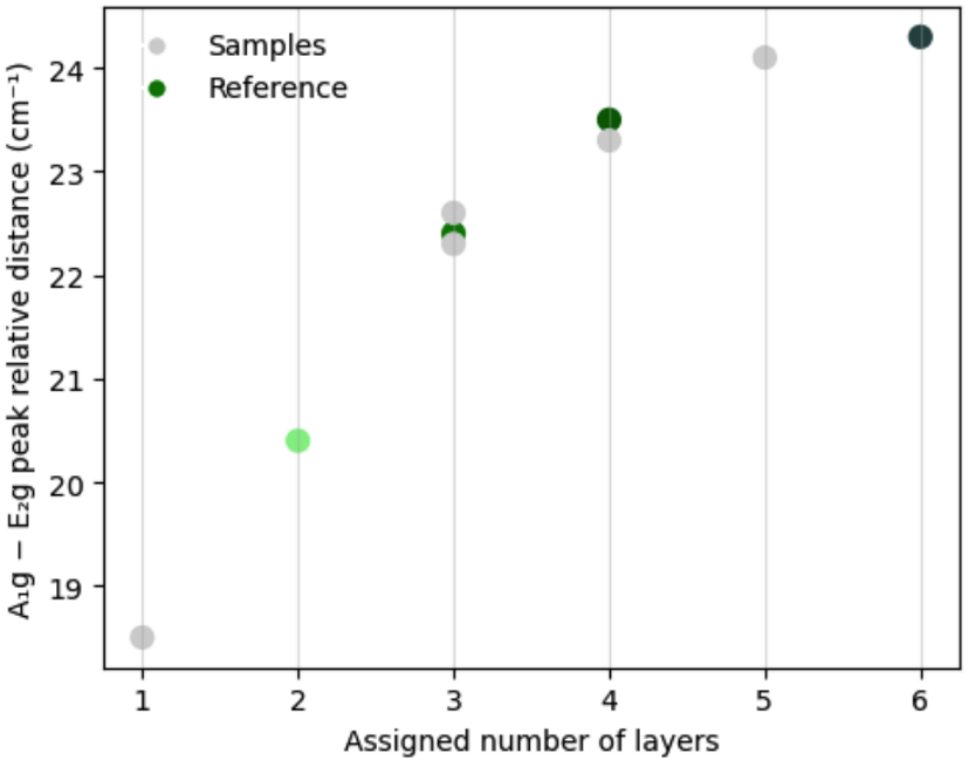

Figure 3.3: **Determination of the MoS_2 layers number in each substrate based on the relative position between A_{1g} and E_{2g}.** The layer number of each sample substrate was assigned by comparing the spectral distance between the A_{1g} and E_{2g} Raman modes with the one measured in the reference flake.

By comparing the measured PL spectra with literature and/or custom-built reference data, and the Raman spectra with those of a reference sample, the number of MoS_2 layers in the substrate of each sample investigated in this work was determined.

3.2. Control of induced strain in WSe_2 through MoS_2 substrate thickness

As discussed in Section 1.2.2, inducing strain in a localized region of WSe_2 monolayers is fundamental to study Single Photon Emission in such systems. As discussed in Section 1.2.4, the samples analyzed in this work have contaminant-based nanobubbles as a source of localized strain within micrometer-scale area, which are located at the interface

between the WSe_2 monolayer and the MoS_2 multilayer (Fig. 3.4-a). The formation of nanobubbles is promoted by annealing [16], which is performed right after stacking WSe_2 on top of MoS_2, as discussed in Section 2.1.
As reported in Figure 3.4-b, to an increase in strain corresponds a redshift in PL emission of WSe_2 monolayers [23]. The strain value corresponding to the redshift of the PL spectra shown in Figure 3.4-b is assigned assuming the nanobubbles to be in biaxial strain condition, and by comparing the spectra to the results reported by Frisenda et al. [20].

To investigate whether the optical response of the nanobubbles can be tuned by choosing the substrate thickness during fabrication, the number of MoS_2 layers present in the substrate of each sample was determined following the process explained in Section 3.1. The average induced redshift within each sample was then plotted as a function of the number of layers in the MoS_2 substrate, as shown in Figure 3.5.

For each fabricated sample, after performing a spatially resolved PL map over the entire sample area, nanobubbles were identified and counted. Each bubble was added to the count as it appeared in the AFM map and if within that same area redshifted PL signal was detected, as reported in Figure 3.4-c,d,e. This was done to avoid counting other type of protuberances, namely contaminant bubbles staying in between the glass and the MoS_2 or on top of the sample itself.

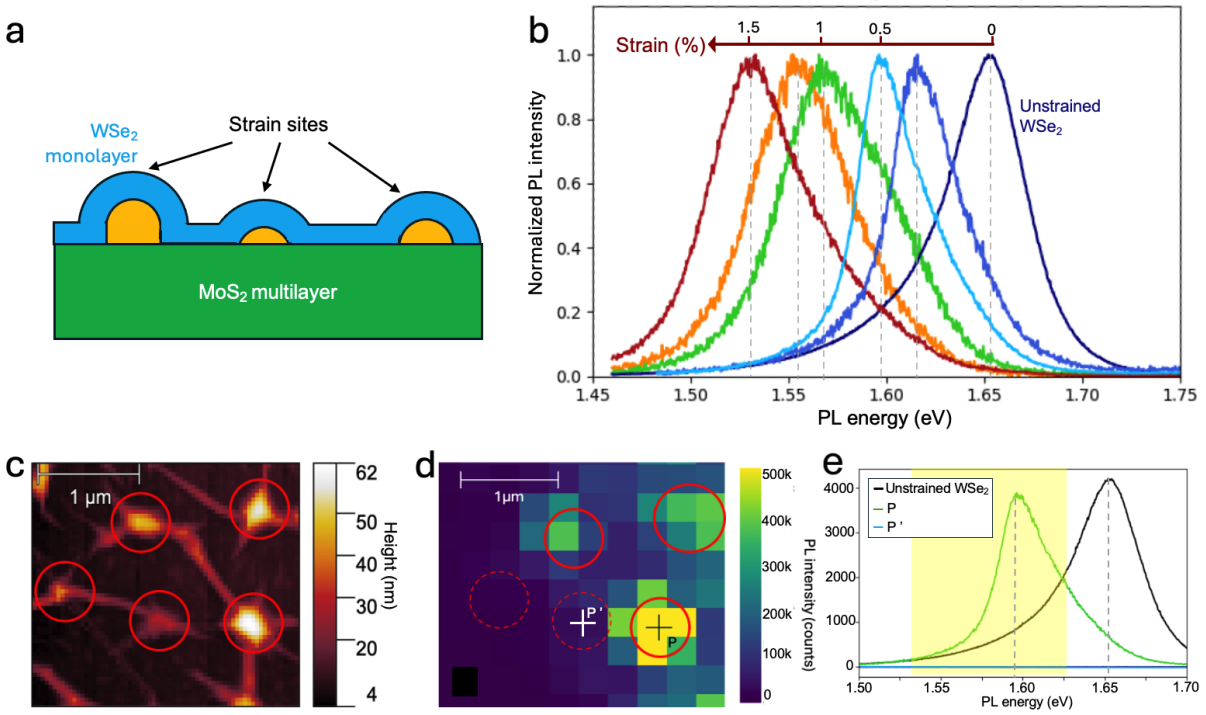

Figure 3.4: **Strain-induced redshift in PL emission of WSe_2 monolayers.** (a) Schematic representation of the samples investigated: contaminant nanobubbles formed at the interface with the MoS_2 substrate induce local strain in WSe_2 monolayer. (b) Shows quantitatively the PL spectrum corresponding to each strain level [20]. In (c) an AFM image of bubbles present in the sample is reported, while in (d) is shown that not all the protuberances detected give PL emission related to strained WSe_2 monolayers. Spectra extracted from (d) are displayed in (e).

From PL measurements of each sample, the emission spectrum of each nanobubble was plotted and the corresponding redshift was extracted by subtracting the PL emission peak position in energy to the unstrained WSe_2 monolayer one at 1.65 eV [52]. A unique distribution was made for samples sharing the same substrate thickness, and the average redshift values were then plotted as a function of the number of MoS_2 layers in the substrate, as shown in Figure 3.5. The average redshift follows an increasing trend with the number of layers, saturating at approximately 110 meV for substrates having 4 layers or more.

A total of 202 nanobubbles distributed in 11 samples were involved in this analysis.

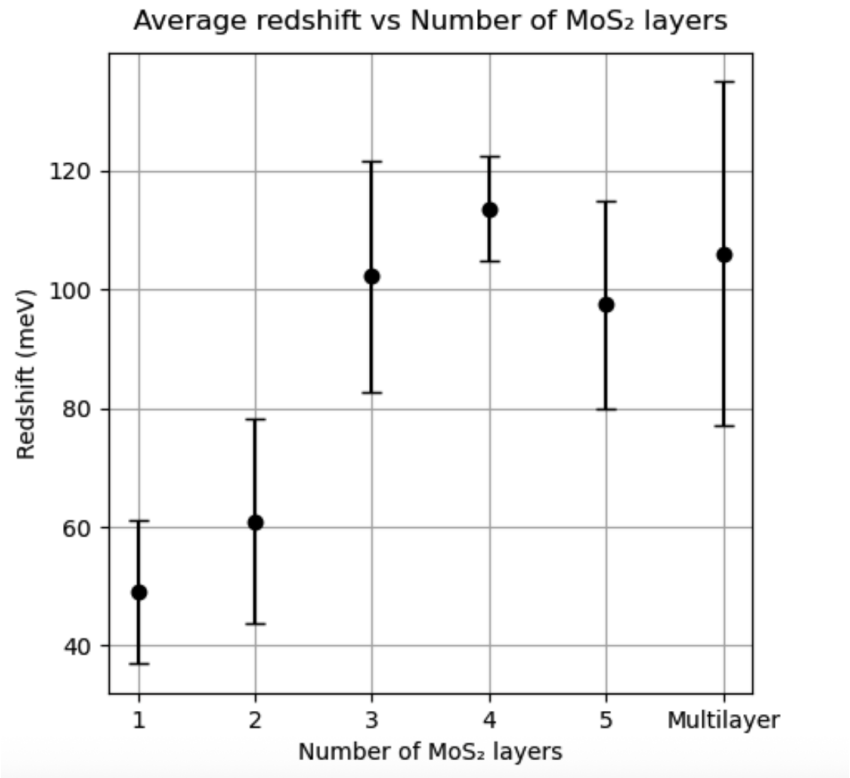

Figure 3.5: **Average nanobubbles redshift on MoS_2 substrate thickness.** Redshift, and thus the strain in the nanobubbles, increases with the number of MoS_2 layers. Nanobubbles on monolayers substrate tend to have redshift values in between 40-60 meV, while for substrates of at least 4 layers the redshift values saturate in between 100 and 120 meV.

3.2.1. Discussion

The increasing trend of induced redshift in the bubbles against the number of MoS_2 layers suggests that the strain acting on each bubble depends on the substrate itself, and that the thicker the substrate is, the more the bubble is strained.
According to Sanchez et al. [46], larger strain in bubbles can arise from stronger adhesion between the monolayer and the substrate, as increased interfacial forces modify the bubble shape.
An apparent correlation between bubble morphology and substrate thickness was observed in the samples investigated in this work. As shown in Figure 3.6, for thin substrates (1-2 layers), the bubbles are usually not isolated, tend to merge together and their shape is irregular. On the other hand, for substrates at least three layers thick, the bubbles are usually isolated, with more regular shape and a rounder profile.

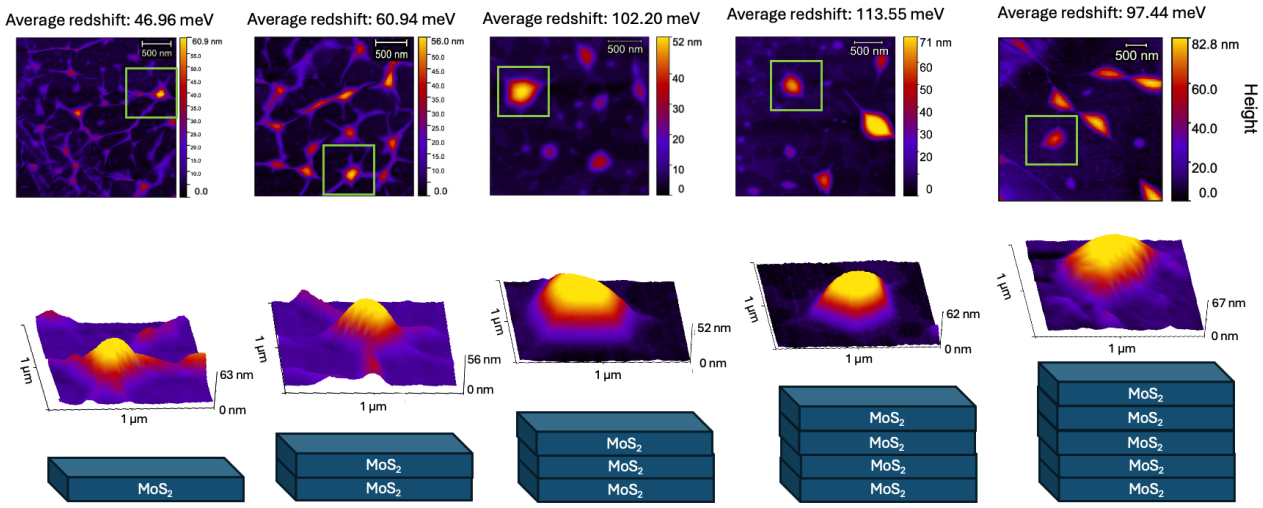

Figure 3.6: **Bubble change in shape with the number of layers in the substrate.** For monolayer and bilayer substrates the bubbles tend to form a network and merge together, and their shape looks more irregular. For thicker substrates the bubbles are isolated and with a rounder shape.

It is important to specify that in the work carried out by Sanchez et al. [46], it was shown how the adhesion forces change the strain in bubbles with circular section by affecting the aspect ratio $\frac{H_m}{R}$, where H_m is the maximum height within the bubble and R is the radius of the base circle. Due to the very irregular shape exhibited by bubbles standing on thin (1-2L) substrates and their tendency to form a network, it was not possible to efficiently investigate the aspect ratio of every sample involved in this work. However, it's possible to observe how the overall morphology of the sample is affected by the substrate thickness, as reported in Figure 3.6.

According to Sanchez et al. [46], what is shown in Figure 3.6 suggests that the adhesion forces in between the WSe_2 and the substrate increase with the number of MoS_2 layers, and this increase in adhesion is what is causing the strain, and thus redshift, to arise.

Björkmann et al. [4] investigated how adhesion forces change in MoS_2 flakes depending on their number of layers. Their results are reported in Figure 3.7, and represented together with the data on average induced redshift previously shown in Figure 3.5. What is being plotted the energy per unit area in meV/Å^2 required to exfoliate one single MoS_2 monolayer from a substrate of N layers of MoS_2 ($E(N)_{XF}$), which is being subtracted to the energy required to separate the monolayer from the bulk ($E(\infty)_{XF}$).

To facilitate the comparison, a fit of the data reported by them was done with a power law. The dashed blue curve plotted is just a guide for the eye, it has no physical meaning.

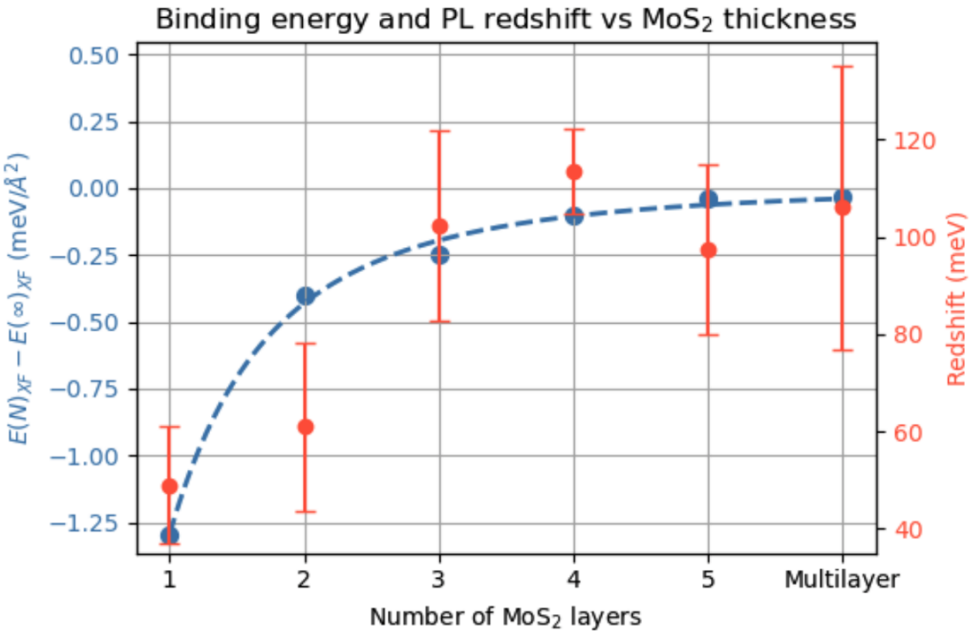

Figure 3.7: **Adhesion energy of MoS_2 substrate and strain induced in the bubbles dependency on the number of MoS_2 layers in the substrate.** Both the plots have a trend of increase and saturate for substrates having four or more layers [4].

As reported, both plots are monotonically increasing and converging to a fixed value, to which they get very close at four layers in the substrate or more.
It is important to specify that Björkmann et al. [4] did not investigate the Van der Waals attractive interactions of various thickness MoS_2 substrates with WSe_2 monolayers, but with MoS_2 monolayers. In the case of WSe_2 monolayers interacting with MoS_2 substrates the plot will be quantitatively different from the one shown in Figure 3.7. However, a similar trend is expected qualitatively, as the the Van der Waals attraction will grow monotonically by adding more layers, as the top monolayer and the bottom layer of the substrate will always be in the attractive regime of the Lennard-Jones potential (Fig. 2.5) [22]. At the same time, the interaction between the top monolayer and the bottom one will become smaller as the number of layers in the substrate, and thus the distance between the two, increases. This will lead to a negligible increase of adhesion energy for bulk substrates, thus to the conversion of the plot of the total adhesion energy at $(E(\infty)_{XF})$, according to its definition.

Based on the data reported by Björkmann et al. [4] and Sanchez et al. [46], and on the experimental data reported in this work (Fig. 3.6, Fig. 3.7) it is possible to conclude that the strain induced in contaminant nanobubbles formed in between a stack of WSe_2 monolayer and a MoS_2 multilayer is directly modulated by the adhesion of the monolayer

with substrate. As schematically represented in Figure 3.8, the adhesion forces act by changing the shape of the bubbles themselves, and grow monotonically with the number of layers present in the substrate.
As strain and PL emission spectra of WSe_2 monolayers are directly correlated (Fig. 3.4-b) [20, 23], it is possible to tune the average optical response of localized emitters by intervening in a fabrication parameter, namely the thickness of the MoS_2 substrate.

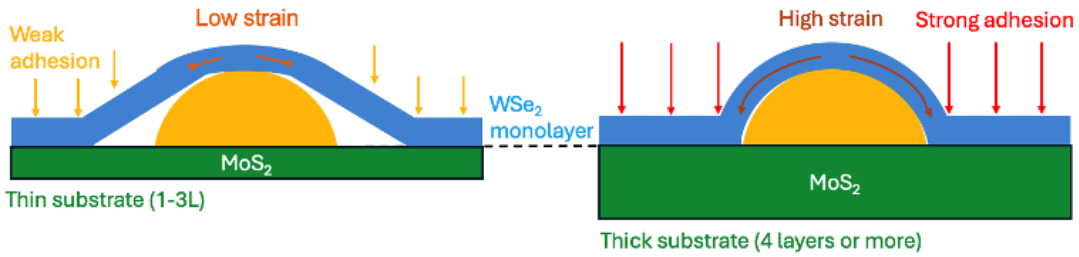

Figure 3.8: **Adhesion-induced deformation in contaminant nanobubbles.** Stronger adhesion related to thicker substrates directly affects the shape of the bubble, leading to higher strain in the monolayer, modulating the PL emission of such system.

3.3. Deterministic nanobubble patterning for Single Photon Emission in WSe_2/MoS_2 stacks

In order to precisely control the final properties of the sample, such as nanobubbles size and density, it is possible to explore alternative fabrication strategies beyond varying the substrate thickness alone. As will be demonstrated in this Chapter, the surface morphology of the sample can be deterministically defined during the fabrication process by employing laser writing on the flakes prior to their transfer.

This approach is particularly relevant from a technological perspective, as devices based on single-photon emitters must be scalable in order to enable practical applications. The ability to deterministically engineer nanobubble arrays therefore represents a promising route toward the realization of efficient, on-demand sources of highly indistinguishable single photons, which are a key requirement for scalable quantum photonic technologies [49].

3.3.1. Initial observation of deterministic nanobubble patterning

During the fabrication and characterization process aimed at obtaining a suitable sample, AFM map revealed the presence of an ordered pattern of round-shaped nanobubbles across the surface, as shown in Figure 3.9. The sample was produced and characterized with the techniques explained in Chapter 2, following these steps:

- Exfoliation of the WSe_2 monolayer on PDMS, with subsequent PL map to make sure that it was a monolayer;
- Exfoliation of the MoS_2 flake on PDMS with subsequent Raman map to determine the number of layers, showing a monolayer region and one having three layers;
- Transfer of the MoS_2 substrate on the glass coverslip and transfer of the WSe_2 monolayer on top;
- PL map of the stack;
- Annealing;
- PL map of the annealed stack;
- AFM characterization;

The spacing of precisely 1µm in between the bubbles in both dimensions, reported in the AFM map showed in Figures 3.9-b,c,d, suggested that the observed pattern could be related to laser writing, occurred while mapping the sample.
As shown in Figures 3.9-e,f the PL map for integration interval 1.53-1.62 eV, thus highlighting the PL emission of strained WSe_2 monolayer, shows hints of a pattern similar to the one found in AFM, suggesting that the bubbles are in between the WSe_2 monolayer and the MoS_2 substrate.
Moreover the PL map taken before the annealing, reported in Figures 3.9-g,h,i, shows how part of the WSe_2 monolayer was already strained, suggesting that the bubbles were there already when the stacking happened.
This led to the idea that the pattern observed is related to laser writing happened when the single flakes were being characterized on PDMS, in which at least one experimental parameter, such as excitation wavelength or the overall laser power, was likely set outside the range typically employed for standard mapping procedures on PDMS.

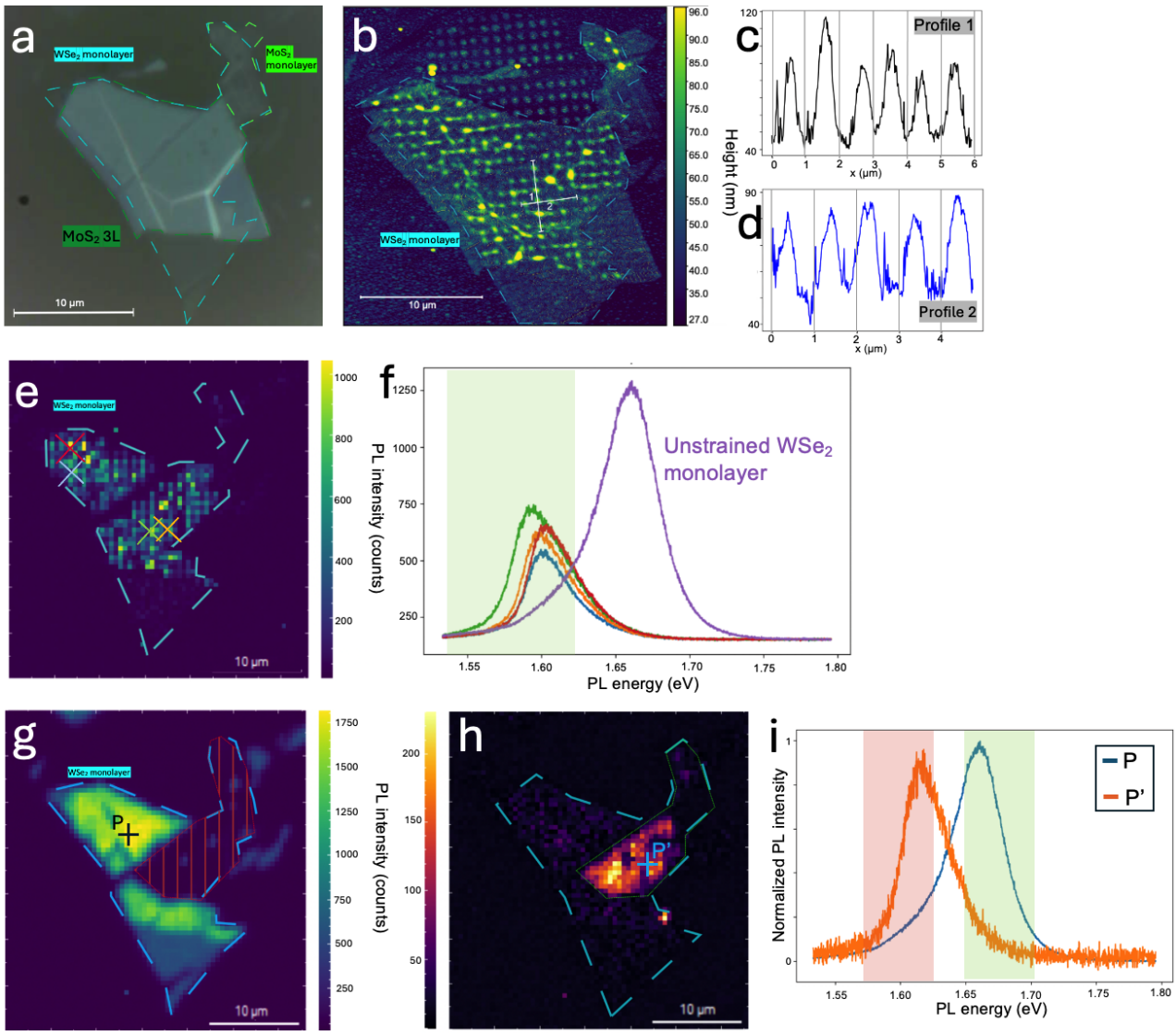

Figure 3.9: **First observation of an ordered nanobubbles array.** (a) Optical microscope image of the WSe_2/MoS_2 stack. (b) AFM image of the sample: the pattern is visible and profiles of it in two orthogonal directions are reported (c,d), both showing a spacing of 1μm between the bubbles. The path of the two profiles can be visualized on the map. (e) PL spectroscopy map of the sample after the annealing. PL spectra extracted all around the heatmap intense areas are reported (f) and compared to the unstrained WSe_2. The integration interval is 1.53-1.62 eV is reported. A pattern similar to the one shown in the AFM map can be observed. (g,h) PL heatmaps of the stack before the annealing for the two different integration intervals reported, namely 1.65-1.7 eV (g) and 1.575-1.625 eV (h). The map in (h) shows how before the annealing PL emission related to to strained WSe_2 monolayers could be detected (i).

3.3.2. Protocol to reproduce nanobubble patterning

Since the controlled reproduction of such patterning could be highly relevant for the scalable fabrication of single-photon emitters [49], the identification of a reliable protocol to reproduce it is of significant interest.
As discussed in Section 3.3.1, the pattern observed for the first time was likely obtained by laser writing one of the flakes before the stacking of these happened. For this reason, the pattern reproduction was attempted by mapping the WSe_2 and MoS_2 flakes separately, to see which method led to the production of a patterned sample.

As a first try, a WSe_2 monolayer was exfoliated on PDMS and characterized by PL mapping using the XploRA setup described in Section 2.3.1. Maps were acquired over different regions of the flake (Fig.3.10-a,b), while varying selected acquisition parameters, such as excitation wavelength and total lasing power, reported in Figure 3.10-c. The chosen power values are more intense then the ones typically involved in PL characterization on PDMS, which are usually in the order of tens of a microwatt. Also different excitation laser wavelengths were used to look if this could lead to different effects. The spatial step size was fixed at 1 µm, as this value was previously shown to produce effective patterning in the initial sample (Fig. 3.9-b), while the acquisition time was kept constant at 0.5 s.
After laser writing, the sample was subsequently transferred onto a glass coverslip and annealed at 200 °C for 12 h.

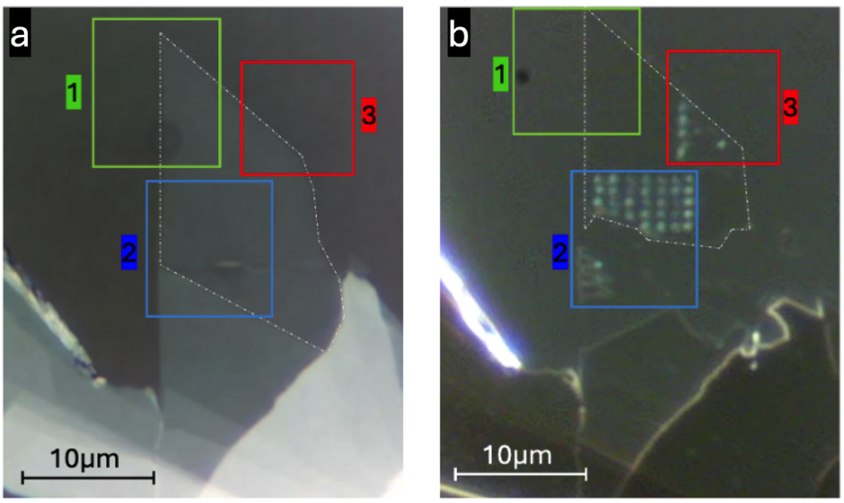

c

Map index	Acquisition parameters	
	Laser wavelength (nm)	Laser power (mW)
1	638 nm	2.4
2	532 nm	1.6
3	532 nm	3.7

Figure 3.10: **Optical microscope image of WSe_2 monolayer and scanning area of different maps.** (a) Bright field image of the flake on PDMS before laser writing. (b) Dark field image of the monolayer after laser writing, transfer on glass substrate and annealing. (c) Table reporting the acquisition parameters used for different maps. The scan spacing and acquisition time were fixed respectively to 1 μm and 0.5 s.

As shown in Figure 3.10-b, in the area where Map 1 was performed, the flake appeared pristine, flat and there seemed to be no laser-induced modification of its morphology. Within the area in which Map 3 was taken there seemed to be signs of an incomplete pattern, but in most of the area the flake appeared to be disrupted. This suggests that the laser beam applied in this region was too powerful. However, in the scanning area of Map 2, the flake featured a an ordered array of spots forming a square lattice, suggesting the presence of deterministically ordered clusters.
Since the lasing power in Map 1 is larger than the one in Map 2 but has a lower wavelength, it is very likely that the patterning happens before a wavelength threshold. On the other hand, it is known that for a lasing power of 0.16 mW by a 532 nm laser (see Table 2.1), no patterning is arising. This is probably because the laser patterning happens after a certain threshold in laser power too.

The scanning area of Map 2 was then characterized by AFM as shown in Figure 3.11-a.

Profiles traced in both dimensions of the 2D ordered array showed a spacing in between the clusters of 1µm, the same spacing as Map 2 (Fig. 3.11-b,c). Within the same region a PL map was performed (Fig. 3.11-d). A decrease in PL intensity was detected in correspondence of the bubbles position, but no strain-induced redshift was observed, as reported in Figure 3.11-e,f.

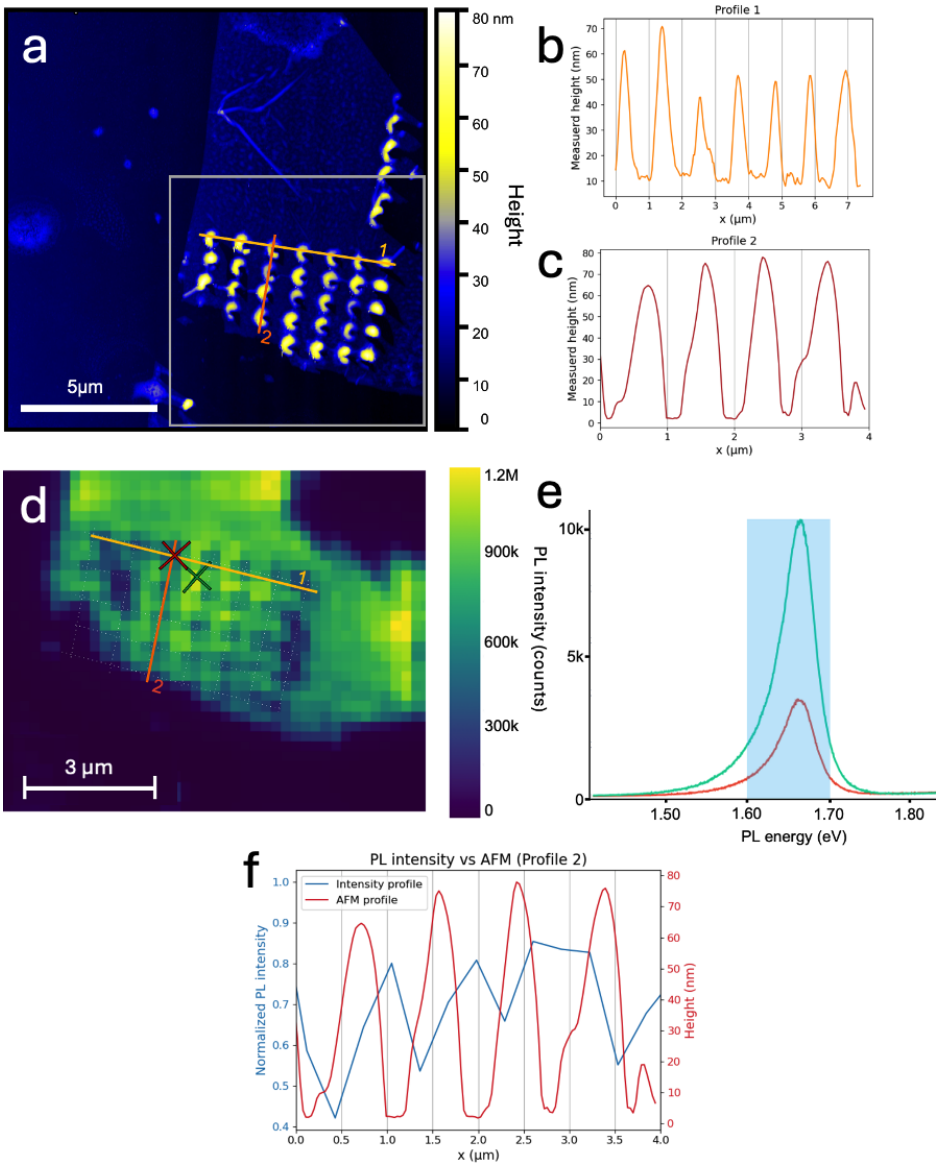

Figure 3.11: **AFM and PL maps on the WSe_2 patterned area.** (a) AFM shows how the spacing in both dimensions of the array (b,c) is consistent with the spacing of the map (1µm). (d) PL map shows that different areas of the pattern have different PL intensity, but no redshift of the emission is being observed (e). (f) The same line profile extracted from the PL heatmap and from the AFM map shows how the intensity drops in correspondence of the patterned bubbles.

Because of the measured intensity inhomogeneity and the absence of strain detection, the nanobubbles are inferred to be located on top of the flake rather than underneath it. This suggests that, before the transfer, the bubbles were located at the interface between the flake and the X4 PDMS stamp, as illustrated in Figure 3.12, and are therefore consistent with being composed of PDMS.

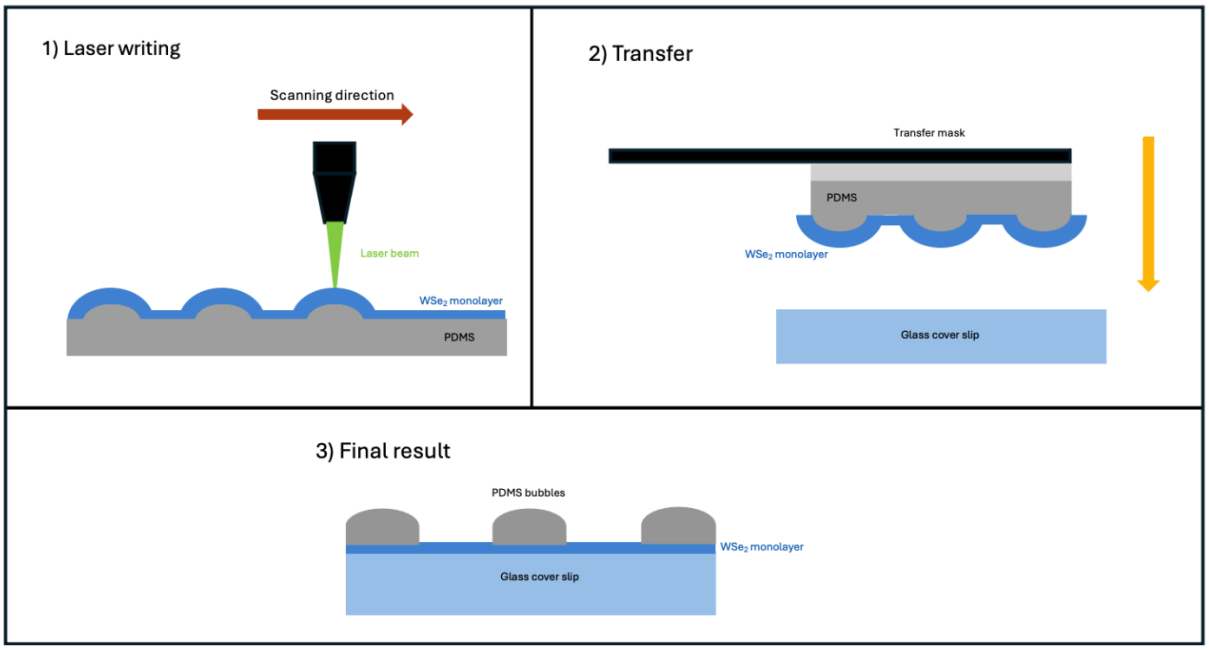

Figure 3.12: **Schematic representation of the proposed patterning process.** The laser writing is assumed to occur in the PDMS layer beneath the flake. This may explain why the nanobubbles are found on top of the flake after the transfer.

Since the pattern forms underneath the flake it can be introduced in a stack at the interface between the WSe_2 monolayer and the MoS_2 substrate only by patterning the MoS_2 flake.

To perform laser writing of the PDMS beneath MoS_2 flakes with thicknesses ranging from one to five layers, the same procedure previously used for patterning WSe_2 monolayers was applied. The selected flake was exposed to a 532 nm laser with an incident power of 1.60 mW (Map 2 in Figure 3.10) and an acquisition time of 0.5 s, leading to the local disruption of the flake. Since in the XploRA Plus setup it was not possible to select a power level in between 0.160 mW, a power which was known to not give any patterning, and 1.60 mW (see Table 2.1), the laser patterning was performed slightly out of focus, to locally decrease the laser power over area. More specifically, the sample surface was brought 2µm above the focus plane. Following this process, signs of patterning on the PDMS beneath the flake were observed by dark-field optical microscopy, as shown in Figure 3.13-a.

To proceed with the heterostructure fabrication, the patterned flake had to be transferred onto a glass substrate, but this step proved to be particularly challenging. MoS_2 flakes subjected to laser patterning were difficult to transfer, and when part of them was transferred, significant damage to both the patterned regions and the flake itself was observed, as shown in Figure 3.13-b. A possible explanation for this behavior can be found in the work of Pandey et al. [42], reporting that the isolation of two-dimensional materials onto corrugated substrates leads to enhanced adhesion, which, in this case, is likely responsible for the observed hindrance of the transfer process. Anyway, the transfer process was less hindered for WSe_2 monolayers with respect to MoS_2 flakes. A possible explanation is that the patterned MoS_2 flakes were more than one layer thick, which would increase their Van der Waals adhesion to the corrugated PDMS substrate [4]. To try to decrease the adhesion of the flake with the substrate by lowering the corrugation, the spacing during laser writing was increased to 2 µm (Fig.3.13-c).

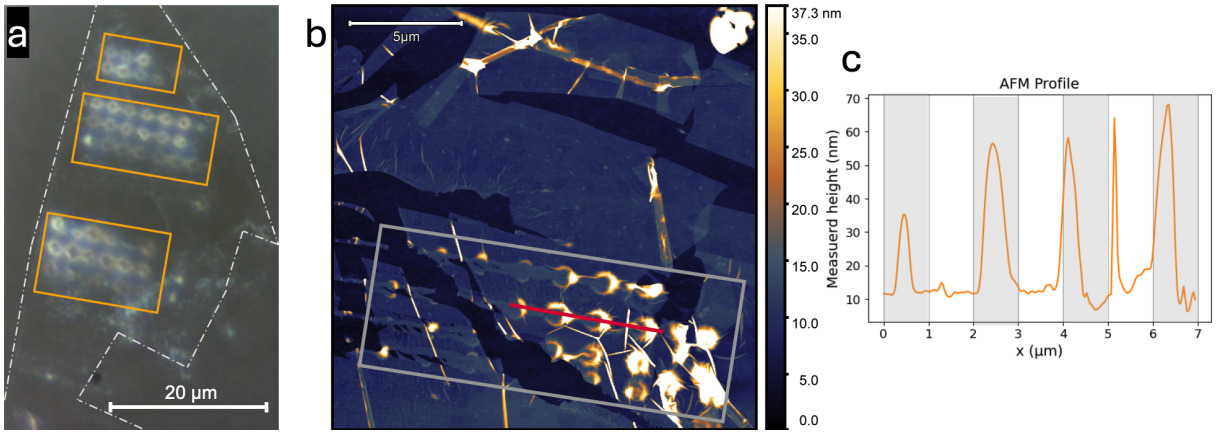

Figure 3.13: **2D array of bubbles with 2µm spacing on MoS_2.** (a) Dark field optical microscope image of laser written MoS_2 flake on PDMS. (b) AFM scan of a nanobubble pattern over an MoS_2 flake after the transfer on glass. The pattern and the flake itself appear damaged. (c) AFM profile shows the 2µm spacing of the pattern.

3.3.3. Discussion and outlook

A suggestion on what is causing the phenomena of round-shaped bubble patterning is found in the work carried out by Naruse et al. [39], in which bubbles of PDMS are formed by laser-writing the uncured liquid polymer focusing a pulsed 532 nm 0.5 ns laser at the interface between the PDMS and a copper plate. The bubbles seem to be made of gaseous species, generated by the high local temperature reached at the PDMS/Cu interface during the laser writing. The bubbles are confined within a membrane, made of thermally-crosslinked PDMS.

In the experiment carried out by Naruse et al. the PDMS before the interaction with the laser is not crosslinked and liquid, unlike the X4 Gel-Pak PDMS involved in this work [39]. However, it's reasonably possible that the round bubble patterning described in this work can be caused by the formation and trapping of gaseous species below the PDMS top surface, induced by the elevated local temperature due to high laser power.
The results reported by Naruse et al. [39] also shows how the dimensions of the bubbles increase linearly together with the lasing power: the height and the radius of the bubbles seem to increase following the same trend. If such behavior was also found in X4 PDMS, it would be possible to tune the shape of the bubbles by choosing the lasing power.

Summarizing what is discussed in this section, it is possible to synthesize the current state of the art of nanobubble patterning in TMDs-based stacks:

- Bubble patterning is possible, and it can be implemented in WSe_2/MoS_2 stacks;
- Bubbles are made of PDMS, and they originate due to interaction of the polymer with a laser beam having power and wavenumber over a certain threshold;
- The threshold in power stands between 0.160 and 1.60 mW;
- The threshold in wavelength is in between 638 and 532 nm;
- It is reasonable to think that the dimensions of the bubbles increase with the laser power;
- To obtain a patterned stack, laser writing must happen on the MoS_2 flake;
- The high adhesion in between the MoS_2 and the corrugated PDMS makes the transfer more difficult. New transfer strategies should be attempted, namely transferring at low temperature to reduce the flake adhesion with the PDMS substrate by thermal contraction of the bubbles.
  Increasing the spacing and lowering the laser power to values closer to the threshold should decrease the corrugation of the substrate, facilitating the transfer.

4 | Optical characterization of nanobubbles

This work aims to understand the physical mechanism governing single photon emission (SPE) heppening in strained WSe_2 monolayers.
In this Chapter, both Tip-enhanced photoluminescence (TEPL) and low temperature confocal PL measurements done on a sample produced according to the methods explained in Section 2.1 are reported. This is done to demonstrate that nanobubbles exhibiting SPE in cryogenic confocal PL maps are the same ones that, when characterized by tip-enhanced photoluminescence (TEPL), display hybridization between defect-related states in WSe_2 and the strain-lowered conduction band occurs, as discussed in Section 1.2.2.
TEPL offers sub-diffraction spatial resolution and can identify the different strain values acting within a nanobubble. Cryogenic confocal PL, although diffraction-limited, is required to resolve narrow emission lines and to assess SPE signatures as such phenomenon does not happen at high temperatures [1].

4.1. Strain characterization of nanobubbles below the diffraction limit

As discussed in Section 2.3.3, TEPL enables optical measurements beyond the diffraction limit, providing PL of individual nanobubbles having up to 10 nm resolution, and thus allowing the reconstruction of the local strain landscape within the bubble [38].
As ongoing research works suggest, SPE may not always happen at the point with the highest strain, thus the bubble apex [12, 14]. TEPL characterization of the bubbles is therefore a crucial step towards understanding SPE in strained WSe_2 monolayers, as it provides direct access to the local strain range over which a nanobubble can host SPE. This type of information is inaccessible for confocal PL characterization.

Figure 4.1 shows the mapping of an individual bubble by TEPL, with a spatial step of

15 nm. The AFM map displayed in Figure 4.1-a shows where the bubble is located within the sample. Figure 4.1-b shows instead the zoomed in AFM scan of such bubble, detected by the AFM system incorporated in the tip-enhanced spectroscopy setup discussed in Section 2.3.3. Such bubble is found both on the three and four layered regions of MoS_2 substrate.

The PL maxima energy positions are displayed, showing that redshift is largest at the center of the bubble and decreases toward the edges, indicating that the maximum tensile strain is localized at the bubble center (Fig. 4.1-c). In addition, spectral signatures consistent with strain-driven hybridization between dark excitonic states and defect-related interband levels are observed within the bubble region. In fact, as reported in Figure 4.1-d, at the edge of the bubble the PL shows two distinguishable peaks at 1.59 eV and 1.55 eV. Such splitting of emission peaks is obtained after hybridization of the energy states, and subsequent avoided crossing. Approaching inner regions of the bubble, and thus increasing the strain, the lower energy peak becomes more intense, dominating the PL emission at the center of the bubble, and the energetic distance between the two peaks increases [23]. As discussed in Section 1.2.2, such hybridization breaks valley symmetry, overcoming spin–orbit coupling selection rule described in Section 1.1.1, and thus allowing radiative recombination in both spin configurations [23, 31]. This explains the increase in PL intensity and contemporary redshift plotted in Figure 4.1-d.

A range of 1-1.2% strain present within the bubble is assigned based on PL peak position and a gauge factor of 100meV/% [20], and comparing the spectral shape to the ones of controlled experiments tracing hybridization [23]. This interval of strain is consistent with the avreage-induced strain in nanobubbles found on three or four layered MoS_2, as reported in Figure 3.5.

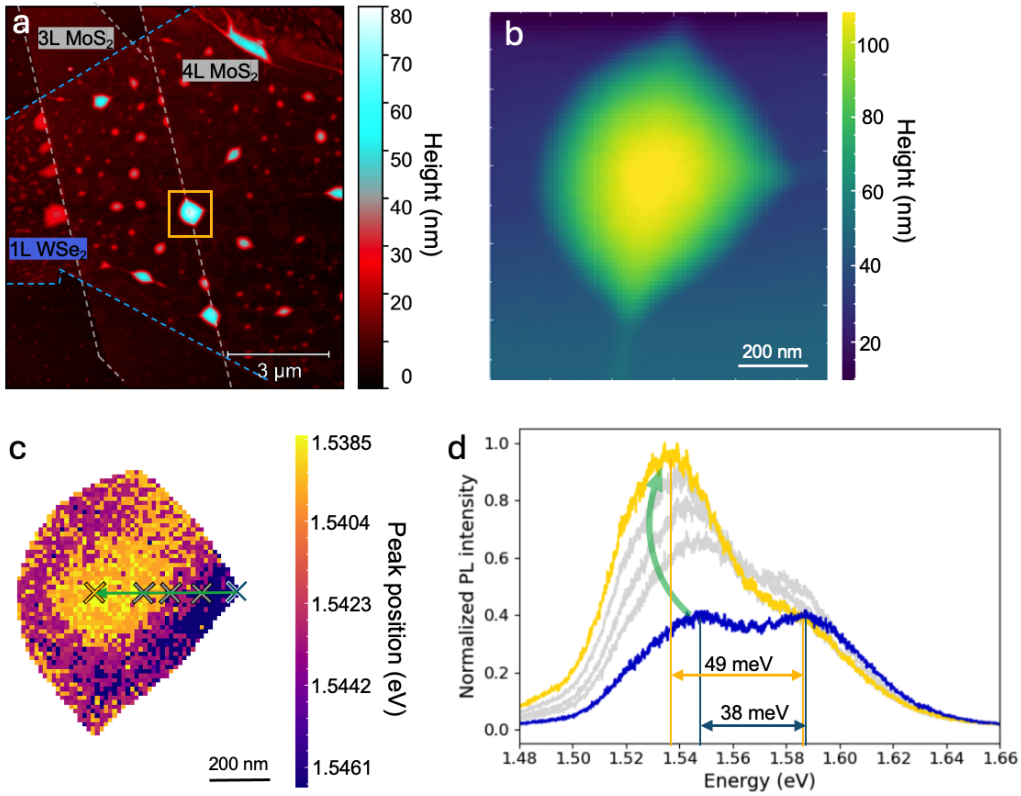

Figure 4.1: **TEPL characterization of a nanobubble.** (a) AFM map shows the bubble location within the WSe_2 monolayer/MoS_2 multilayer stack, while (b) shows the zoomed in AFM map of the bubble, extracted from the TEPL scan. (c) TEPL scan of the blister, the peak position in energy is plotted. It is shown how larger redshift is present at the center of the bubble. A mask was applied to the original TEPL map, referring to the AFM reported in (b). In this way, only the pixels corresponding to the actual bubble are shown. (d) Spectra extracted at different distances from the bubble center, the spatial position of each spectrum is marked in (c). Spectral signatures of strain-driven hybridization described in Section 1.2.2 occurring within the bubble are observed.

4.2. Towards Single-Photon Emission: Photoluminescence spectroscopy of locally strained WSe_2 monolayer with decreasing temperatures

This work aims to demonstrate single-photon emission in strained WSe_2 monolayers originates from the efficient recombination of electron–hole pairs, allowed by strain-induced hybridization of dark excitons with interband defect-related states, as discussed in Section 1.2.2 [31]. For this reason, the sample containing the bubble shown in Figure 4.1

was characterized by low-temperature photoluminescence in order to detect SPE and to compare the emitting sites with their TEPL characterization.

By performing low-temperature confocal photoluminescence maps, the nanobubbles previously characterized by TEPL could be identified. As shown in Figure 4.2-a,b, the AFM scan (a) is being compared to the PL map of the sample at 15K (b), having integration interval 1.5-1.7 eV.
This procedure was applied to the bubble presented in Figure 4.1, which is being highlighted and marked as Bubble 1 in Figure 4.2, enabling the measurement of its PL spectrum over a temperature range from room temperature down to 15 K, immediately before the SPE onset [1]. The sample was analyzed in such temperature range to search for signatures of potential single-photon emitters at lower temperatures.

Blisters having a strain range of 1-1.2% and exhibiting exciton–defect hybridization within itself, such as Bubble 1, display PL emission at room temperature associated with different recombination mechanisms, including both bright and dark excitonic states [23]. This low-hybridization regime is therefore investigated in order to determine whether SPE can occur under such conditions.
PL spectra at various temperatures of Bubble 1 are reported in Figure 4.2-c. Each spectrum plotted was normalized by the maximum PL intensity value of unstrained WSe_2 at that temperature. It is possible to notice how at lower temperatures the PL emission of both the bubble and the unstrained WSe_2 monolayer peaks are found at higher energies. This is consistent with the thermal-induced bandgap widening featured by WSe_2 monolayers, discussed in Section 1.2.1 [25].
The ratio in between the bubble and the unstrained WSe_2 intensity maxima was calculated for every temperature and plotted as a function of it, showing significant increase approaching lower temperatures, and exceeding 1 at 15 K (Fig. 4.2-d).
While the increase in PL intensity at low temperature is not sufficient to demonstrate single-photon emission, it motivates further investigation at lower temperatures, as enhanced brightness is frequently observed in quantum emitters under cryogenic conditions [1].

A second bubble, standing on three layers of MoS_2, is highlighted as Bubble 2 in Figure 4.2-a,b and its PL spectra at different temperatures are reported in Figure 4.2-e. The spectra have been normalized with respect to the most intense value among all of them and displayed separated one from another to help their visualization. It is possible to see how the PL intensity increases markedly upon lowering the temperature, consistent with an enhancement of radiative recombination, while the emission peak undergoes a blueshift, reflecting once again the thermal-induced widening of the bandgap in WSe_2

monolayers [25].

As a consequence of inhibition of PL emission thermal broadening, two comparatively sharp and intense peaks arise from the spectra at 15 K (Fig. 4.2-e). This observation motivates further low-temperature investigation, as is consistent that such spectral features could evolve into quantum emission lines at lower temperature.

Room-temperature confocal PL measurements on Bubble 2 revealed an emission peak at 1.56 eV, which is consistent with the presence of exciton–defect hybridization within the bubble [20, 23]. Such energy position of the PL peak is also compatible with the result reported in Figure 3.5, showing that nanobubbles standing on 3L MoS_2 have average PL peak position at 1.56 eV

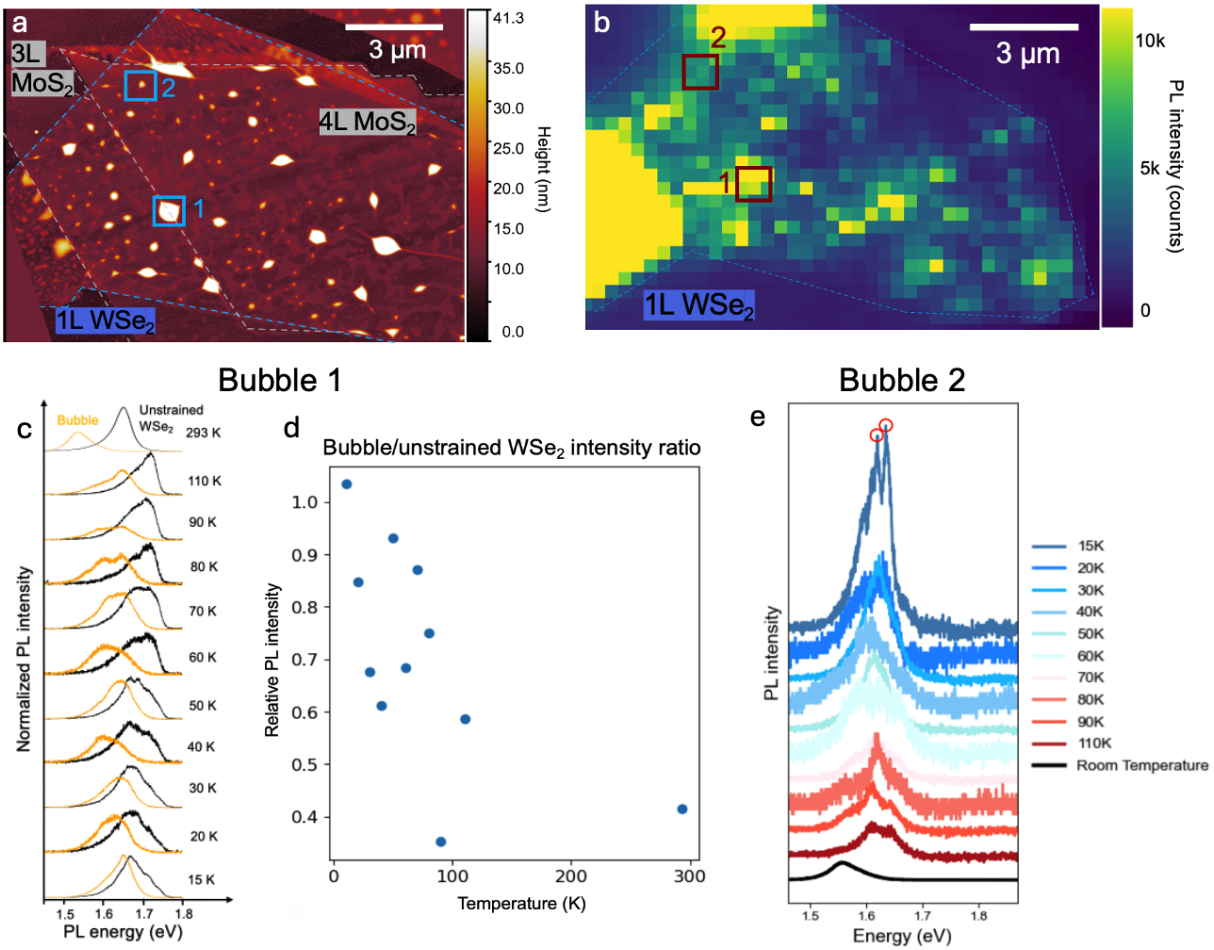

Figure 4.2: **Temperature dependency of PL emission in nanobubbles.** AFM map of the sample (a) is compared to a PL map performed at 15K (b), having integration interval 1.5-1.7 eV. Several bubbles within the sample can be identified, and two of them are highlighted. (c) PL emission plot of both Bubble 1 and the unstrained WSe_2 a different temperatures. (d) Bubble 1/unstrained WSe_2 PL intensity ratio as a function of temperature. (e) PL spectra of Bubble 2 at different temperatures. At 15K two intense and sharp peaks highlighted in the plot seem to arise.

4.3. Discussion

As discussed in Section 1.2.2, for 1-1.2% strain in WSe_2 monolayers, hybridization between dark excitonic states and defect-related interband levels occurs. Such hybridization breaks valley symmetry, overcoming spin–orbit coupling selection rule and thus allowing radiative recombination in both spin configurations [23, 31]. The increase in oscillator strength related to such hybridization may explain the high brightness commonly observed in single-photon emitters [5, 33].

Temperature dependence of the same system was studied up to 15K, immediately before the SPE onset [1]. As reported in Figures 4.1 and 4.2, two bubbles within the analyzed sample proved to be potential single-photon emitters at low temperatures, both showing signs compatible with dark exciton-defect states hybridization occurring at room temperature. The presence of such hybridization is inferred from the observation that, at least in part of the bubbles, the PL peak is located at 1.56 eV, corresponding to an estimated tensile strain of approximately 1%, a regime in which hybridization has been reported to occur [23].
Direct experimental proof that hybridization between dark excitons and defect-related states is the mechanism responsible for single-photon emission has not yet been established; nevertheless, this scenario appears to be a promising explanation for the observed phenomena. To further clarify the underlying mechanisms, the next steps should be:

- Reaching lower temperatures (<10K);
- Measure second order correlation function ($g^{(2)}(\tau)$) for localized emitters and identification of bubbles showing SPE;

Once the strain range required for the formation of single-photon emitters in WSe_2 monolayers is identified, WSe_2/MoS_2 stacks exhibiting such strain values within their nanobubbles can be deliberately fabricated by selecting the substrate thickness, as discussed in Section 3.2 and shown in Figure 3.5.

5 | Conclusions and future developments

This work investigated strain engineering in WSe_2 monolayers stacked on multilayer MoS_2 substrates as a platform for single-photon emission. The primary objective was to explore the correlation between locally induced strain, generated by contaminant-driven nanobubbles, and the activation of spectrally sharp emission features associated with quantum emitters.

The first part of this work focused on the fabrication of strain engineered samples with tunable strain via substrate choice and deterministically placement via laser writing. An optimized fabrication protocol was developed to produce samples exhibiting localized strain in WSe_2 monolayers, such that signs compatible with SPE could be observed within these systems. The process involves exfoliation of WSe_2 onto PDMS, followed by transfer onto multilayer MoS_2 (1–5 layers), which was either exfoliated directly onto a glass coverslip or first exfoliated onto PDMS and subsequently transferred onto glass. The stacks were then annealed to promote bubble formation and strain localization [16]. The fabrication procedure is described in detail in Section 2.1.

A systematic methodology was implemented to accurately determine the thickness of the MoS_2 substrates in terms of layer number, as detailed in Section 3.1. The analysis combines photoluminescence spectroscopy (PL), atomic force microscopy (AFM), and Raman spectroscopy. In particular, the layer number was extracted from the evolution of the characteristic Raman modes E^1_{2g} and A_{1g}, whose spectral separation increases with the number of layers [29]. The Raman shift difference between these two modes was used as a primary indicator of thickness, and the assignment was further corroborated by AFM step-height measurements and PL signatures. The final layer determination was performed by comparison with a calibrated MoS_2 reference sample fabricated and characterized specifically for this purpose (Fig. 3.1).

The characterization of the fabricated samples indicates that the average strain induced in WSe_2 blisters increases as a function of the MoS_2 substrate thickness, exhibiting a satura-

tion behavior for substrates comprising four or more layers, as reported in Figure 3.5. As discussed in Section 3.2.1, this trend can be attributed to the increase in adhesion forces experienced by the monolayer as the number of substrate layers increases [4]. Enhanced adhesion modifies the morphology of individual blisters [46], as illustrated in Figure 3.6, leading to a change in their shape and a corresponding increase in the induced strain.
While carrying out this work, a patterning protocol aimed at deterministically controlling bubble nucleation sites was introduced in Section 3.3. At the current state of the art, bubble formation is known to happen due to laser writing on the PDMS layer beneath the TMD flake. This process has been observed for an optical power of approximately 1.60 mW in a 532 nm laser; however, the precise power and wavelength thresholds have not yet been precisely determined. Once these parameters are identified, the dependence of bubble morphology on laser power, wavelength, and laser exposure time should be investigated in order to achieve controlled and reproducible strain engineering.

The second part of the work investigated the microscopic mechanism behing SPE.
To have the full picture of what was the strain landscape within each bubble, TEPL measurements were performed on blisters, providing the strain distribution by performing PL spectroscopy with nanometer resolution. Figure 4.1 reports hints of the strain–driven hybridization discussed in Section 1.2.2 occurring within nanobubbles.
The TEPL map of such blisters was then compared to their PL evolution with temperature down to 15 K, close to the SPE onset [1]. It was observed how some bubbles exhibited spectral features consistent with the emergence of single-photon emitters upon further cooling. More specifically, one exhibited sharp and intense PL peaks at 15 K, which are likely to evolve into localized emitter lines upon reaching the typical SPE onset temperature. At room temperature, this bubble already showed signatures consistent with strain-induced hybridization, with its PL maximum observed at 1.56 eV (Fig. 4.2-e). These observations suggest that single-photon emission in WSe_2 monolayers may originate from strain-induced hybridization between dark excitons and defect-related states, although additional experimental evidence is required to conclusively validate this mechanism.
To further investigate this hypothesis, measurements must be performed at temperatures below 10 K, using cryogenic confocal PL [1]. Once this condition is achieved, single-photon emitters should be identified by measuring the second-order correlation function $g^{(2)}(\tau)$ and selecting emitters that satisfy the criterion $g^{(2)}(0) < 0.5$ [30].
For each confirmed emitter, the corresponding TEPL characterization should be analyzed in order to determine the strain range at room temperature associated with the occurrence of SPE.

It should be noted that the strain range associated with single-photon emission at low temperature may not directly correspond to the strain conditions under which hybridization is observed at room temperature. Weakly hybridized bubbles at room temperature could undergo partial or complete de-hybridization upon cooling. This may occur due to the temperature dependence of the bandgap, which increases at lower temperatures (Fig. 1.5, [24]), thereby modifying the energetic alignment between excitonic and defect states. In addition, differences in the thermal expansion coefficients of the TMD and the contaminant trapped within the bubble could lead to a temperature-dependent strain redistribution. At present, however, no experimental evidence demonstrates such de-hybridization in weakly hybridized bubbles.

Once the room-temperature strain range associated with single-photon emission at cryogenic temperatures has been identified, samples containing bubbles featuring this strain window can be fabricated by appropriately selecting the substrate thickness, as discussed in Section 3.2.

To achieve deterministic positioning of strain-engineered bubbles within a device, the PDMS bubble patterning process described in Section 3.3 requires further investigation, in particular to determine the power threshold for bubble formation and the parameters governing bubble size and morphology.

If the strain induced on the WSe_2 monolayers by patterned bubbles follows the same substrate-thickness dependence outlined in Section 3.2, this approach could enable deterministic spatial placement of emitters with substrate-tuned strain, providing a viable route toward integration in practical devices.

Bibliography

[1] R. Ai, X. Cui, and Y. Li. Local strain engineering of two-dimensional transition metal dichalcogenides towards quantum emitters. *Nano-Micro Letters*, 2025. doi: https://doi.org/10.1007/s40820-024-01611-1.

[2] W. Ali, Y. Liu, M. Huang, Y. Xie, and Z. Li. Temperature-dependent phonon scattering and photoluminescence in vertical mos2/wse2 heterostructures. *Nanomaterials*, 13(16), 2023. ISSN 2079-4991. doi: 10.3390/nano13162349. URL https://www.mdpi.com/2079-4991/13/16/2349.

[3] B. Alunda and Y. Lee. Review: Cantilever-based sensors for high speed atomic force microscopy. *Sensors*, 20:4784, 08 2020. doi: 10.3390/s20174784.

[4] T. Björkman, A. Gulans, A. V. Krasheninnikov, and R. M. Nieminen. van der waals bonding in layered compounds from advanced density-functional first-principles calculations. *Phys. Rev. Lett.*, 108:235502, Jun 2012. doi: 10.1103/PhysRevLett.108.235502. URL https://link.aps.org/doi/10.1103/PhysRevLett.108.235502.

[5] A. Branny, S. Kumar, and R. Proux. Deterministic strain-induced arrays of quantum emitters in a two-dimensional semiconductor. *Nature Communication*, 2017. doi: https://doi.org/10.1038/ncomms15053.

[6] R. A. Bromley, R. B. Murray, and A. D. Yoffe. The band structures of some transition metal dichalcogenides. iii. group via: trigonal prism materials. *Journal of Physics C: Solid State Physics*, 5(7):759, apr 1972. doi: 10.1088/0022-3719/5/7/007. URL https://doi.org/10.1088/0022-3719/5/7/007.

[7] Y. Cao and M. Sun. Tip-enhanced raman spectroscopy. *Reviews in Physics*, 8:100067, 2022. ISSN 2405-4283. doi: https://doi.org/10.1016/j.revip.2022.100067. URL https://www.sciencedirect.com/science/article/pii/S2405428322000016.

[8] A. Castellanos-Gomez, M. Buscema, R. Molenaar, V. Singh, L. Janssen, H. S. J. van der Zant, and G. A. Steele. Deterministic transfer of two-dimensional materials by all-dry viscoelastic stamping. *2D Materials*, 1(1):011002, apr 2014. doi: 10.1088/2053-1583/1/1/011002. URL https://doi.org/10.1088/2053-1583/1/1/011002.

[9] K. R. Castleman and I. T. Young. *Microscope Image Processing*. Elsevier Science, 2 edition, 2022.

[10] J. Chen, X. Xie, S. Li, Z. Liu, J.-T. Wang, J. He, and Y. Liu. Layer-resolved ferromagnetic and antiferromagnetic proximity effects in crps4/wse2 heterostructures. *The Journal of Physical Chemistry Letters*, 2025. doi: 10.1021/acs.jpclett.5c02670. URL https://doi.org/10.1021/acs.jpclett.5c02670.

[11] M. Chhowalla, H. S. Shin, G. Eda, L.-J. Li, K. P. Loh, and H. Zhang. The chemistry of two-dimensional layered transition metal dichalcogenide nanosheets. *Nature Chemistry*, 5, 2013. doi: 10.1038/nchem.1589.

[12] Z. Dai, Y. Hou, D. A. Sanchez, G. Wang, C. J. Brennan, Z. Zhang, L. Liu, and N. Lu. Interface-governed deformation of nanobubbles and nanotents formed by two-dimensional materials. *Phys. Rev. Lett.*, 121:266101, Dec 2018. doi: 10.1103/PhysRevLett.121.266101. URL https://link.aps.org/doi/10.1103/PhysRevLett.121.266101.

[13] J. Dang, S. Sun, X. Xie, Y. Yu, K. Peng, C. Qian, S. Wu, F. Song, J. Yang, S. Xiao, L. Yang, Y. Wang, M. A. Rafiq, C. Wang, and X. Xu. Identifying defect-related quantum emitters in monolayer wse2. *npj 2D Materials and Applications*, 2020. doi: 10.1038/s41699-020-0136-0. URL https://doi.org/10.1038/s41699-020-0136-0.

[14] T. Darlington, C. Carmesin, and M. Florian. Imaging strain-localized excitons in nanoscale bubbles of monolayer wse2 at room temperature. *Nature Nanotechnology*, 2020.

[15] M. W. Doherty, N. B. Manson, P. Delaney, F. Jelezko, J. Wrachtrup, and L. C. Hollenberg. The nitrogen-vacancy colour centre in diamond. *Physics Reports*, 528(1):1–45, 2013. ISSN 0370-1573. doi: https://doi.org/10.1016/j.physrep.2013.02.001. URL https://www.sciencedirect.com/science/article/pii/S0370157313000562. The nitrogen-vacancy colour centre in diamond.

[16] K. Du, B. Qiao, X. Ding, C. Huang, and H. Hu. Bubbles in 2d materials: Formation mechanisms, impacts, and removal strategies for next-generation electronic devices. *Nanomaterials*, 15(24), 2025. doi: 10.3390/nano15241888. URL https://www.mdpi.com/2079-4991/15/24/1888.

[17] M. D. Eisaman, J. Fan, A. Migdall, and S. V. Polyakov. Invited review article: Single-photon sources and detectors. *Review of Scientific Instruments*, 82(7):071101, 07 2011. ISSN 0034-6748. doi: 10.1063/1.3610677. URL https://doi.org/10.1063/1.3610677.

[18] M. Esmann, S. C. Wein, and C. Antón-Solanas. Solid-state single-photon sources: Recent advances for novel quantum materials. *Advanced Functional Materials*, 34 (30):2315936, 2024. doi: https://doi.org/10.1002/adfm.202315936. URL `https://advanced.onlinelibrary.wiley.com/doi/abs/10.1002/adfm.202315936`.

[19] FabNS. Empowering optical spectroscopy. URL `https://www.fabns.com.br/`.

[20] R. Frisenda, M. Drüppel, R. Schmidt, S. Michaelis de Vasconcellos, D. Perez de Lara, R. Bratschitsch, M. Rohlfing, and A. Castellanos-Gomez. Biaxial strain tuning of the optical properties of single-layer transition metal dichalcogenides. *npj 2D Materials and Applications*, 2017. doi: 10.1038/s41699-017-0013-7.

[21] P. A. F. Garrillo. *Development of highly resolved and photo-modulated Kelvin probe microscopy techniques for the study of photovoltaic systems.* PhD thesis, Université Grenoble Alpes, 1 2019.

[22] F. J. Giessibl. Advances in atomic force microscopy. *Reviews of Modern Physics*, 75: 949–970, 2003. doi: 10.1103/RevModPhys.75.949.

[23] P. Hernández López, S. Heeg, C. Schattauer, S. Kovalchuk, A. Kumar, D. J. Bock, J. N. Kirchhof, B. Höfer, K. Greben, D. Yagodkin, L. Linhart, F. Libisch, and K. I. Bolotin. Strain control of hybridization between dark and localized excitons in a 2d semiconductor. *Nature Communications*, 2022. doi: 0.1038/s41467-022-35352-9. URL `https://doi.org/10.1038/s41467-022-35352-9`.

[24] J. Huang, T. B. Hoang, and M. H. Mikkelsen. Probing the origin of excitonic states in monolayer wse2. *Scientific Reports*, 2016. doi: 10.1038/srep22414. URL `https://doi.org/10.1038/srep22414`.

[25] J. Jadczak, J. Kutrowska-Girzycka, P. Kapuściński, Y. Huang, A. Wójs, and L. Bryja. Probing of free and localized excitons and trions in atomically thin wse2, ws2, mose2 and mos2 in photoluminescence and reflectivity experiments. *Nanotechnology*, 2017. doi: 10.1088/1361-6528/aa87d0.

[26] A. Jorio, R. Nadas, A. G. Pereira, C. Rabelo, A. C. Gadelha, T. L. Vasconcelos, W. Zhang, Y. Miyata, R. Saito, M. D. D. Costa, and L. G. Cançado. Nano-raman spectroscopy of 2d materials. *2D Materials*, 11(3):033003, may 2024. doi: 10.1088/2053-1583/ad42ad. URL `https://doi.org/10.1088/2053-1583/ad42ad`.

[27] J. Kim, K. Jeong, S. Kwon, J. So, M. Wang, P. Snapp, H. Park, and S. Nam. Strained two-dimensional tungsten diselenide for mechanically tunable exciton transport. *Nature Communications*, 2024. doi: 10.1038/s41467-024-55135-8.

[28] D. Lazić. *Short Instructions for Raman Microscope Horiba Xplora*, pages 199–206. Ubiquity Press, 07 2019. ISBN 9781911529521. doi: 10.5334/bbj.q.

[29] R. Lewandowska. *Number of layers of MoS2 determined using Raman Spectroscopy*. Horiba, 2014. URL `https://www.horiba.com/fileadmin/uploads/Scientific/Documents/Raman/RA54.pdf`.

[30] X. Lin, X. Dai, C. Pu, Y. Deng, Y. Niu, L. Tong, W. Fang, Y. Jin, and P. X. Electrically-driven single-photon sources based on colloidal quantum dots with near-optimal antibunching at room temperature. *Nature Communications*, 2017. doi: 10.1038/s41467-017-01379-6.

[31] L. Linhart, M. Paur, V. Smejkal, J. Burgdörfer, T. Mueller, and F. Libisch. Localized intervalley defect excitons as single-photon emitters in wse_2. *Phys. Rev. Lett.*, 123: 146401, Sep 2019. doi: 10.1103/PhysRevLett.123.146401. URL `https://link.aps.org/doi/10.1103/PhysRevLett.123.146401`.

[32] N. Lundt. *Strong light-matter coupling with 2D materials*. PhD thesis, 01 2019.

[33] Y. Luo, G. Shepard, J. Ardelean, D. Rhodes, B. Kim, K. Barmak, J. Hone, and S. Strauf. Deterministic coupling of site-controlled quantum emitters in monolayer wse2 to plasmonic nanocavities. *Nat Nanotechnol.*, 2018. doi: 10.1038/s41565-018-0275-z.

[34] K. F. Mak, C. Lee, J. HONE, J. Shan, and T. F. Heinz. Atomically thin mos2: A new direct-gap semiconductor. *Physical Review Letters*, 2010. doi: 10.1103/PhysRevLett.105.136805.

[35] K. F. Mak, C. Lee, J. Hone, J. Shan, and T. F. Heinz. Atomically thin mos_2: A new direct-gap semiconductor. *Phys. Rev. Lett.*, 105:136805, Sep 2010. doi: 10.1103/PhysRevLett.105.136805. URL `https://link.aps.org/doi/10.1103/PhysRevLett.105.136805`.

[36] L. M. Malard, L. Lafeta, R. S. Cunha, R. Nadas, A. Gadelha, L. G. Cançado, and A. Jorio. Studying 2d materials with advanced raman spectroscopy: Cars, srs and ters. *Phys. Chem. Chem. Phys.*, 23:23428–23444, 2021. doi: 10.1039/D1CP03240B. URL `http://dx.doi.org/10.1039/D1CP03240B`.

[37] S. Manzeli, D. Ovchinnikov, D. Pasquier, O. V. Yazyev, and A. Kis. 2D transition metal dichalcogenides. *Nature Reviews Materials*, 2(8):17033, Aug. 2017. doi: 10.1038/natrevmats.2017.33.

[38] R. B. Nadas. *Tip-Enhanced Raman Spectroscopy and Photoluminescence in Two-Dimensional Systems*. PhD thesis, Universidade Federal de Minas Gerais, 8 2024.

[39] T. Naruse and Y. Hanada. Rapid, high-quality microfabrication of thermoset polymer pdms using laser-induced bubbles. *Opt. Express*, 27(7):9429–9438, Apr 2019. doi: 10.1364/OE.27.009429. URL https://opg.optica.org/oe/abstract.cfm?URI=oe-27-7-9429.

[40] K. S. Novoselov, D. Jiang, F. Schedin, T. J. Booth, V. V. Khotkevich, S. V. Morozov, and A. K. Geim. Two-dimensional atomic crystals. *Proceedings of the National Academy of Sciences*, 102(30):10451–10453, 2005. doi: 10.1073/pnas.0502848102. URL https://www.pnas.org/doi/abs/10.1073/pnas.0502848102.

[41] C. Palacios-Berraquero, D. M. Kara, A. R.-P. Montblanch, M. Barbone, P. Latawiec, D. Yoon, A. K. Ott, M. Loncar, A. C. Ferrari, and M. Atatüre. Large-scale quantum-emitter arrays in atomically thin semiconductors. *Nature Communications*, 2017. doi: 10.1038/ncomms15093. URL https://doi.org/10.1038/ncomms15093.

[42] M. Pandey, B. Parida, M. Ranjan, R. Ahuja, and R. Kumar. Pinning of graphene for conformal wrinkling over a soft corrugated substrate through prestretch-release process. *Applied Surface Science Advances*, 16:100433, 2023. ISSN 2666-5239. doi: https://doi.org/10.1016/j.apsadv.2023.100433. URL https://www.sciencedirect.com/science/article/pii/S2666523923000685.

[43] M. S. Rana, H. Pota, and I. Petersen. Improvement in the imaging performance of atomic force microscopy: A survey, 03 2016.

[44] S. Ren, Q. Tan, and J. Zhang. Review on the quantum emitters in two-dimensional materials. *Journal of Semiconductors*, 40(7):071903, jul 2019. doi: 10.1088/1674-4926/40/7/071903. URL https://doi.org/10.1088/1674-4926/40/7/071903.

[45] P. Rivera, H. Yu, K. L. Seyler, N. P. Wilson, W. Yao, and X. Xu. Interlayer valley excitons in heterobilayers of transition metal dichalcogenides. *Nature Nanotechnology*, 2018. doi: 10.1038/s41565-018-0193-0. URL https://doi.org/10.1038/s41565-018-0193-0.

[46] D. A. Sanchez, Z. Dai, P. Wang, A. Cantu-Chavez, C. J. Brennan, R. Huang, and N. Lu. Mechanics of spontaneously formed nanoblisters trapped by transferred 2d crystals. *Proceedings of the National Academy of Sciences*, 115(31):7884–7889, 2018. doi: 10.1073/pnas.1801551115. URL https://www.pnas.org/doi/abs/10.1073/pnas.1801551115.

[47] P. Senellart, G. Solomon, and A. White. High-performance semiconductor quantum-dot single-photon sources. *Nature Nanotechnology*, 2017. doi: 10.1038/nnano.2017.218. URL https://doi.org/10.1038/nnano.2017.218.

[48] P. Senellart, G. Solomon, and A. White. High-performance semiconductor quantum-dot single-photon sources. *Nature Nanotechnology*, 2017. doi: 10.1038/nnano.2017.218. URL https://doi.org/10.1038/nnano.2017.218.

[49] N. Somaschi, V. Giesz, L. De Santis, J. C. Loredo, M. P. Almeida, G. Hornecker, S. L. Portalupi, T. Grange, C. Antón, J. Demory, C. Gómez, I. Sagnes, N. D. Lanzillotti-Kimura, A. Lemaítre, A. Auffeves, A. G. White, L. Lanco, and P. Senellart. Near-optimal single-photon sources in the solid state. *Nature Photonics*, 10(5):340–345, Mar. 2016. ISSN 1749-4893. doi: 10.1038/nphoton.2016.23. URL http://dx.doi.org/10.1038/nphoton.2016.23.

[50] R. M. Stöckle, Y. D. Suh, V. Deckert, and R. Zenobi. Nanoscale chemical analysis by tip-enhanced raman spectroscopy. *Chemical Physics Letters*, 318(1):131–136, 2000. ISSN 0009-2614. doi: https://doi.org/10.1016/S0009-2614(99)01451-7. URL https://www.sciencedirect.com/science/article/pii/S0009261499014517.

[51] SuperTran. St-500 series microscopy cryostats. URL https://www.lakeshore.com/products/product-detail/janis/st-500-microscopy-cryostat?srsltid=AfmBOopAtU216nSuMKrXD1ZpFxoK7WeGrKocrTaVv9HE0RoFZ3RLAJ9g.

[52] P. Tonndorf, R. Schmidt, P. Böttger, X. Zhang, J. Börner, A. Liebig, M. Albrecht, C. Kloc, O. Gordan, D. R. T. Zahn, S. M. de Vasconcellos, and R. Bratschitsch. Photoluminescence emission and raman response of monolayer mos2, mose2, and wse2. *Opt. Express*, 21(4):4908–4916, Feb 2013. doi: 10.1364/OE.21.004908. URL https://opg.optica.org/oe/abstract.cfm?URI=oe-21-4-4908.

[53] M. Turunen, M. Brotons-Gisbert, Y. Dai, Y. Wang, E. Scerri, C. Bonato, K. D. Jöns, Z. Sun, and B. D. Gerardot. Quantum photonics with layered 2d materials. *Nature Reviews Physics*, 2022. doi: 10.1038/s42254-021-00408-0. URL https://doi.org/10.1038/s42254-021-00408-0.

[54] T. L. Vasconcelos, B. S. Archanjo, B. S. Oliveira, W. F. Silva, R. S. Alencar, C. Rabelo, C. A. Achete, A. Jorio, and L. G. Cançado. Optical nanoantennas for tip-enhanced raman spectroscopy. *IEEE Journal of Selected Topics in Quantum Electronics*, 27(1), 2021. doi: 10.1109/JSTQE.2020.3008526.

[55] P. Verma. Tip-enhanced raman spectroscopy: Technique and recent advances. *Chem-*

ical Reviews, 117(9):6447–6466, 2017. doi: 10.1021/acs.chemrev.6b00821. URL https://doi.org/10.1021/acs.chemrev.6b00821. PMID: 28459149.

[56] G. Wang, A. Chernikov, M. M. Glazov, T. F. Heinz, X. Marie, T. Amand, and B. Urbaszek. Colloquium: Excitons in atomically thin transition metal dichalcogenides. *Rev. Mod. Phys.*, 90:021001, Apr 2018. doi: 10.1103/RevModPhys.90.021001. URL https://link.aps.org/doi/10.1103/RevModPhys.90.021001.

[57] J. Wilson and A. Yoffe. The transition metal dichalcogenides discussion and interpretation of the observed optical, electrical and structural properties. *Advances in Physics*, 18(73):193–335, 1969. doi: 10.1080/00018736900101307. URL https://doi.org/10.1080/00018736900101307.

[58] Z. Wu and Z. Ni. Spectroscopic investigation of defects in two-dimensional materials. *Nanophotonics*, 6(6):1219–1237, 2017. doi: doi:10.1515/nanoph-2016-0151. URL https://doi.org/10.1515/nanoph-2016-0151.

[59] O. V. Yazyev and A. Kis. Mos2 and semiconductors in the flatland. *Materials Today*, 18(1):20–30, 2015. ISSN 1369-7021. doi: https://doi.org/10.1016/j.mattod.2014.07.005. URL https://www.sciencedirect.com/science/article/pii/S1369702114002557.

[60] B. Zhu, X. Chen, and X. Cui. Exciton binding energy of monolayer ws2. *Scientific Reports*, 2015. doi: 10.1038/srep09218. URL https://doi.org/10.1038/srep09218.

List of Figures

List of Tables

Acknowledgements

The past two years have been extremely enriching, both from a personal and a professional perspective. I am grateful for the opportunity to study and work at a high-level institution such as Politecnico di Milano, as well as for the chance to carry out this work abroad in an academic, international, and stimulating environment like the PLD group at Humboldt Universität zu Berlin.

In this regard, I would like to express my sincere gratitude to my professor and advisor, Carlo Spartaco Casari, whose support made this experience possible. I would also like to thank the PLD group for welcoming me and supporting my work throughout this thesis, with special thanks to Dr. Sebastian Heeg and Pablo Hernandez Lopez, who followed me step by step during this journey.

Last but not least, I would like to thank my family and friends for their constant support and encouragement. This achievement would not have been possible without them.